

# Comparison of General Circulation Models of the Venus upper atmosphere

Antoine Martinez<sup>a,b</sup>, Hiroki Karyu<sup>c</sup>, Amanda Brecht<sup>d</sup>, Gabriella Gilli<sup>a</sup>,  
Sebastien Lebonnois<sup>b</sup>, Takeshi Kuroda<sup>c</sup>, Aurelien Stolzenbach<sup>a</sup>, Francisco  
González-Galindo<sup>a</sup>, Stephen Bouger<sup>d</sup>, Hitoshi Fujiwara<sup>e</sup>

<sup>a</sup>*Instituto de Astrofísica de Andalucía (IAA-CSIC) Glorieta de la Astronomía  
s/n, Granada, 18008, Spain*

<sup>b</sup>*Laboratoire de Meteorologie Dynamique (LMD) CNRS, Jussieu, Box  
99, Paris, 75252, France*

<sup>c</sup>*Graduate School of Science Tohoku University, Sendai, 980-8578, Japan*

<sup>d</sup>*Ames Research Center Space Science Division National Aeronautics and Space  
Administration (NASA) Moffett Field, California, USA*

<sup>e</sup>*Faculty of Science and Technology Seikei University, Tokyo, 180-8633, Japan*

---

## Abstract

In the context of future Venusian missions, it is crucial to improve our understanding of Venus upper atmosphere through 3D modeling, notably for spacecraft orbit computation. This study compares three General Circulation Models (GCMs) of the Venusian atmosphere up to the exosphere: the Venus Planetary Climate Model (Venus PCM), the Venus Thermospheric Global Model (VTGCM) and the Tohoku University GCM (TUGCM), focusing on their nominal simulations (e.g. composition, thermal structure and heating/cooling rates). Similarities and discrepancies among them are discussed in this paper, together with data-models comparison. The nominal simulations analyzed in this study fail to accurately reproduce the daytime observations of Pioneer Venus, notably overestimating the exospheric temperature. This is linked to an underestimation of the atomic oxygen (O) abundance in the three GCMs, and suggests the need of additional O production in the thermosphere. The selection of solar spectrum is also the main reason for the discrepancies between the models in terms of temperature dependence on solar activity. A list of recommendations is proposed aiming at improving the modeling of Venus' upper atmosphere, among them: 1. Standardize the EUV-UV solar spectrum input. 2. Update the near-infrared heating scheme with Venus Express-Era data. 3. Reassess Radiative cooling

schemes. 4. Investigate the underestimated atomic Oxygen abundance.

*Keywords:* Venus, Venus atmosphere, Venus structure

*PACS:* 0000, 1111

*2000 MSC:* 0000, 1111

---

## 1. Introduction

The Venusian thermosphere, located between 120 km and the exobase (250 km on the dayside, 200 km on the nightside), is distinct from Mars' or Earth's thermospheres, particularly due to extremely cold temperature on the nightside, known as the cryosphere. This cold layer is mainly caused by CO<sub>2</sub> 15  $\mu$ m radiative cooling and by gravity waves (GW), which slow down winds above 110 km and thus reduce adiabatic heating (Schubert et al., 1980; Martinez et al., 2023). Due to its low density, the thermosphere is highly sensitive to solar EUV radiation, which controls both composition (e.g. by photochemistry) and temperature. Venus' low eccentricity and inclination lead to negligible seasonal effects. The atmosphere below 110 km consists mostly of CO<sub>2</sub> (96.5%) and of N<sub>2</sub> (3.5%), but above this altitude solar radiation dissociates CO<sub>2</sub>, making atomic oxygen dominant above 140-155 km, depending on solar activity. The Venusian thermosphere has been observed by a few missions aimed at improving our understanding of its structure and physical processes, and characterizing some of its properties. Key missions studying the Venusian thermosphere include:

- Pioneer Venus (PV, 1978-1982): during high solar activity, provided foundational data on composition, temperature and mass density, mainly above 140 km (Niemann et al., 1980; Hedin et al., 1983; Keating et al., 1985).
- Magellan (1990-1994) and Venus Express (VEx, 2008-2014) missions carried out aerobraking campaigns in the 1990 (Giorgini et al., 1995; Tolson et al., 2013) and 2010 (Persson, 2015; Müller-Wodarg et al., 2016), respectively, to estimate mass density at various solar cycle phases (intermediate and low). Venus Express also made some observations of composition between 80 and 130-140 km altitude (Persson, 2015; Gilli et al., 2015; Vandaele et al., 2016; Mahieux et al., 2012; Limaye et al., 2017).

These data are of importance given the difficulty to make in situ observations of the Venusian atmosphere between 100 and 150 km. On one hand, the atmosphere is too dense for an orbiter to make in situ measurements. On the other hand, it is not dense enough for indirect observations, resulting in a lack of data and coverage for this altitude range, usually with large uncertainty. Therefore, numerical modeling is essential. Starting with the pioneer work by Young and Pollack (1977), 48 years ago, modeling of Venus' upper atmosphere has always been a challenge. In the last decade, GCMs have made important efforts in predicting and understanding the characteristics of the Venusian atmosphere, from the deep atmospheric structure to the thermospheric/ionospheric activity (e.g., Brecht et al., 2011; Brecht et al., 2021; Hoshino et al., 2012, 2013; Sugimoto et al., 2014; Lebonnois et al., 2016; Mendonça and Read, 2016; Yamamoto, 2019; Gilli et al., 2017, 2021; Navarro et al., 2021; Stolzenbach et al., 2023; Martinez et al., 2023, 2024).

This study is part of the Venus Climate Database (VCD) project, a tool freely available online, designed for engineers and scientists in need of reference atmosphere for mission planning, observations preparation, analysis, and interpretation (<http://www-venus.lmd.jussieu.fr/>). The current VCD version is based on outputs from simulations using the Venus Planetary Climate Model (Venus PCM or VPCM; Martinez et al., 2023, 2024), with future versions aiming to incorporate other 3D models' output. For instance, the Venus Thermospheric Global Climate Model (VTGCM; Brecht et al., 2011; Brecht et al., 2021) and Tohoku University Global Climate Model (TUGCM; Hoshino et al., 2012, 2013) focus on the Venus thermosphere and can be used as alternative scenario providers for VCD. Our goal is to understand inter-model differences to improve reliability for future Venus exploration.

In this paper, Section 2 presents the three reference models mentioned above, and the main physical processes of the thermosphere. The differences in the parameterization of these processes will be highlighted. The results of the comparison of thermal and dynamical structure and neutral composition among the three reference simulations is presented in Section 3. Comparison to observational and reconstructed data by Pioneer Venus, Venus Express and Magellan mission is done in Section 4. Section 5 presents the conclusions of the study, with recommendations on the requirements for model development and the need for further observations.

## 2. GCMs description

The section presents the three different 3D models used in the inter-comparison study, with the main references and characteristics summarized in the Table 1.

	VPCM	VTGCM	TUGCM
References	Lebonnois et al. (2010); Gilli et al. (2017, 2021); Martinez et al. (2023, 2024)	Bougher et al. (1999); Brecht et al. (2011); Brecht and Bougher (2012); Brecht et al. (2021)	Hoshino et al. (2013, 2012)
Physical variables	T, U, V, W; CO <sub>2</sub> , N <sub>2</sub> , CO, O + photochemical model (Stolzenbach et al., 2023) + ionospheric model (Martinez et al., 2024)	T, U, V, W; CO <sub>2</sub> , N <sub>2</sub> , CO, O, N <sup>4</sup> S, N <sup>2</sup> D, NO, O <sub>2</sub> , SO, SO <sub>2</sub> , Photochemical Equilibrium ions	T, U, V, W; CO <sub>2</sub> , CO, O
Composition (vmr)	96.5% of CO <sub>2</sub> and 3.5% of N <sub>2</sub>	96.5% of CO <sub>2</sub> and 3.5% of N <sub>2</sub>	100% of CO <sub>2</sub>
Pressure range (number of levels)	9.2×10 <sup>6</sup> Pa to 8.9×10 <sup>-9</sup> Pa (90)	4440 Pa to 1×10 <sup>-9</sup> Pa (69)	356 Pa to 6×10 <sup>-7</sup> Pa (38)
Lower boundary	Topography	Venus Flexible Modeling System GCM: T, U, V, Z, five days averaged outputs (~70 km)	Fixed conditions at 80 km (Hoshino et al., 2012)
Horizontal resolution (Lat x Lon)	1.875° x 3.75°	5° x 5°	T21 (~5.6° x 5.6°)
Temporal discretization	Leapfrog-Matsuno scheme Physical timestep: 210s	Leapfrog scheme Physical timestep: 20s	Leapfrog scheme Physical timestep: 4s

Table 1: Summary of the characteristics of the GCMs used in this work. See text for more details.

### Venus Planetary Climate Model (VPCM; formerly IPSL Venus GCM)

The Venus PCM has been developed at "Laboratoire de Météorologie Dynamique" for more than 20 years (Lebonnois et al., 2010) in collaboration with LATMOS (Sorbonne University, Paris) and IAA-CSIC (Granada, Spain). It has received several modeling improvements in the last 5 years and has been used to investigate all regions of the Venusian atmosphere, as

it covers the surface up to the exobase (200-250 km; Lebonnois et al., 2016; Gilli et al., 2017, 2021; Martinez et al., 2023, 2024). The model solves the primitive equation of hydrodynamics on a sphere, using a finite difference discretization scheme which conserves both potential enstrophy for barotropic non-divergent flow, and total angular momentum for axisymmetric flow. The model provides temperature, neutral and ion composition, winds (zonal, meridional and vertical), mass mixing ration, among other atmospheric variables.

Contrary to Lebonnois et al. (2010), the physical timestep is  $\sim 210$  seconds (1/48000th of solar Venusian day; 116.75 Earth day) and the dynamical timestep is ten times shorter than the physical timestep ( $\sim 21$ s). The horizontal resolution is  $3.75^\circ \times 1.875^\circ$  (96 longitudes  $\times$  96 latitudes) and the vertical grid has 90 pressure levels covering from  $\sim 9.2 \times 10^6$  Pa (surface) to  $\sim 8 \times 10^{-9}$  Pa (250 km at noon and 200 km at midnight, approximately at high solar activity; E10.7 = 200 solar flux unit (s.f.u)). The vertical grid is not regular, with a higher resolution close to the surface. The vertical model resolution is approximately  $\sim 2$ -3 km between 100 and 150 km, slightly smaller below 100 km and  $\sim 4$ -10 km above 150 km (0.01-0.4 scale height below 100 km and 0.4-0.8 scale height above). Conditions at the model upper boundary are similar to previous versions of the Venus PCM (sponge layer over the top four layers, with horizontal winds forced towards zonal average fields with a timescale of the order of 1 Earth day in the top layer).

The configuration and the initial state used in the presented work are based on Martinez et al. (2023, 2024), except that the photolysis rate of CO<sub>2</sub> into CO and O(<sup>1</sup>D) is not tuned "ad-hoc" to fit PV-ONMS density observations as proposed in Martinez et al. (2023). The atmospheric composition above the surface is 96.5% of CO<sub>2</sub> and 3.5% of N<sub>2</sub> (volume mixing ratio). This version of Venus PCM includes a complete photochemical model of the Venus atmosphere and a simplified cloud microphysics (Stolzenbach et al., 2023), with the recent inclusion of ion chemistry and nitrogen chemistry (Martinez et al., 2024) that allows us to simulate both O<sub>2</sub>(a<sup>1</sup> $\Delta$ ) and NO airglow emissions.

## Venus Thermospheric Global Climate Model (VTGCM)

The VTGCM is a 3-D finite-difference hydrodynamic model of the Venus upper atmosphere (e.g., Bouger et al., 1988). It started from the National Center for Atmospheric Research (NCAR) terrestrial Thermospheric Iono-

sphere General Circulation Model (Dickinson et al., 1981). Over the last few decades, the VTGCM has been modified and improved with the details documented in Bouger et al. (1988), Brecht (2011), Brecht et al. (2011), Brecht and Bouger (2012), Bouger et al. (2015) and Brecht et al. (2021).

The model calculates neutral temperature, zonal velocity, meridional velocity, mass mixing ratio of specific species, vertical motion, and geopotential. The VTGCM solves the time-dependent primitive equations for the neutral atmosphere. The diagnostic equations (hydrostatic and continuity) provide geopotential and vertical motion. Additionally, the prognostic equations (thermodynamic, eastward momentum, northward momentum, and composition) are solved for steady state solutions for the temperature, zonal (eastward) velocity, meridional (northward) velocity, and mass mixing ratio of specific species. These equations have been described in detail by Bouger et al. (1988) even if the primed (perturbation) values have been replaced by total field values. The VTGCM spatial dimensions are 5° by 5° latitude-longitude grid (72 longitudes x 36 latitudes), with 69 evenly-spaced log-pressure levels in the vertical (from 4440 Pa to 1 nPa), extending from approximately  $\sim$ 70–300 km ( $\sim$ 70–200 km) at local noon (midnight) and at high solar activity. The vertical resolution is half a pressure height scale, which is equivalent to  $\sim$ 3–5 km. The temporal discretization uses a leap-frog scheme with a timestep of 20 seconds. The major species calculated are CO<sub>2</sub>, CO, O, N<sub>2</sub>, and the minor species are O<sub>2</sub>, N(<sup>4</sup>S), N(<sup>2</sup>D), NO, SO, and SO<sub>2</sub>. The major species influence the atmospheric mean mass, temperature, and global scale winds, while the minor species are passive tracers (i.e., do not change the mean mass, temperature, or winds). The minor species are set according to the global averaged values given by Yung and Demore (1982). Selected dayside photochemical ions are carried to support the neutral chemistry (CO<sub>2</sub><sup>+</sup>, O<sub>2</sub><sup>+</sup>, O<sup>+</sup>, N<sub>2</sub><sup>+</sup>, and NO<sup>+</sup>) and are in photochemical equilibrium. The latest ion-neutral reactions and rates used in the VTGCM are largely taken from Fox and Sung (2001). For the top boundary, VTGCM uses the Fourier and Shapiro filter that assumes:  $\frac{dT}{dz} = 0$ ,  $\frac{dU}{dz} = \frac{dV}{dz} = \frac{dW}{dz} = 0$  and the composition is in diffusive equilibrium.

The lower boundary for the VTGCM is set at a single pressure slice at  $4.44 \times 10^3$  Pa from the Venus Flexible Modeling System (FMS) GCM (Lee and Richardson, 2010, 2011). The lower boundary consists of latitude versus longitude maps for temperature, zonal wind, meridional wind, and geopotential height. The Venus FMS GCM output is zonally averaged and is temporally averaged over 5 solar days so that each longitude point represents

a diurnal average of the data at that fixed longitude (Brecht et al., 2021). This spatially-varying lower-boundary condition only impacts the temperature and winds up to 80 km, with the largest impact at 70 km. The VTGCM is typically executed in a continuation start (warm start) but when it was originally designed the initial conditions were global mean profiles for temperatures and CO<sub>2</sub>, CO, N<sub>2</sub>, O from the Global Empirical Model of The Venus Thermosphere (VTS3) by Hedin et al. (1983) (see Bouger et al., 1988). The VTGCM simulations presented in this paper are continued (warm started) from the simulation number 5 published in Brecht et al. (2011).

### Tohoku University General Circulation Model (TUGCM)

The TUGCM is a 3-D Venusian mesosphere and thermosphere GCM whose basic features are based on Bouger et al. (1988). It predicts distributions of temperature, wind velocity, and number density (O, CO, CO<sub>2</sub>) by solving the primitive equations, continuity equation, and energy conservation equation in the sigma-coordinate system (Hoshino et al., 2013). The dynamical core is based on the spectral transform method, instead of the compact finite difference. Photochemical reactions including CO<sub>2</sub> photolysis, formation of O<sub>2</sub>, and CO<sub>2</sub> recombination are taken into account for the atmospheric composition calculation (Hoshino et al., 2012).

The altitude region extends from 356 Pa ( $\sim$ 80 km) to about  $6 \times 10^{-7}$  Pa ( $\sim$ 190 km at noon and  $\sim$ 150 km at midnight, at high solar activity) which is divided into 38 vertical layers. The horizontal spatial resolution is a triangular truncation of T21 (common spectral grid resolution method), which is equivalent to  $\sim$ 5.6° longitude by  $\sim$ 5.6° latitude (64 longitudes x 32 latitudes), and the vertical resolution is set at 0.5 scale height (Hoshino et al., 2013). At the lower boundary, the temperature is fixed at 196 K across all latitudes and longitudes (Seiff et al., 1985). The horizontal and vertical wind velocities are assumed to be 0 m/s at this boundary.

The initial state of the simulation is assumed to be an atmosphere at rest. The initial temperature and number density (CO, CO<sub>2</sub> and O) distributions are taken from VTS3 by Hedin et al. (1983), which represents the Venusian upper atmosphere during a solar maximum.

#### *2.1. GCMs configuration of main thermospheric processes*

Parameterizations for CO<sub>2</sub> 15  $\mu$ m cooling, molecular diffusion, near-infrared (NIR) heating, extreme ultraviolet heating, and sub-grid processes (i.e., eddy

diffusion, viscosity, and conduction) are included and discussed in more detail in Brecht et al. (2011) and Brecht and Bouger (2012) for VTGCM, in Gilli et al. (2017, 2021) and Martinez et al. (2023, 2024) for VPCM and in Hoshino (2011); Hoshino et al. (2012, 2013) for TUGCM. The aim of this section is to present the similarities and differences in references and parameterizations of the main physical processes of the thermosphere for each model (see Table 2). The effect of these differences on the thermal structure, winds and composition will be discussed in the next section.

### 2.1.1. *CO<sub>2</sub> photochemistry*

Thermospheric chemistry is mainly controlled by the photodissociation and photoionization of CO<sub>2</sub>, which are the main reactions in the upper atmosphere. CO<sub>2</sub> interacts efficiently with the EUV-UV solar spectrum between 0.1 and 225 nm (with photoionization for wavelengths below 85 nm and photodissociation above). The range and intensity of the solar spectrum used, as well as the quantum yield (or quantum efficiency) of the reactions, will therefore have an impact on the modeling of the Venusian upper atmosphere.

- VPCM photodissociates CO<sub>2</sub> into CO and O approximately from 85 to 210 nm with a quantum efficiency of 1. Below 85 nm, this quantum yield is reduced and depends on the quantum yield of photoionization.
- VTGCM photodissociates CO<sub>2</sub> into CO and O approximately from 85 to 225 nm with a quantum efficiency of 1 (Dickinson and Bouger, 1986). Below 85 nm, the quantum yield is reduced and depends on the quantum yield of photoionization.
- For TUGCM, photodissociation of CO<sub>2</sub> into CO and O is calculated between 100 nm and 200 nm with a quantum yield of 1 for  $\lambda \geq 167$  nm and 0.5 for  $\lambda \leq 167$  nm (Hoshino, 2011; Hoshino et al., 2012).

Note that the choice of the factor of 0.5 for TUGCM is taken from Inn and Heimerl (1971), but the observed yield is closer to 1 (Felder et al., 1970; Stief et al., 1969; Clark and Noxon, 1970). As a consequence, CO<sub>2</sub> photodissociation should be 2 times less efficient at wavelengths below 167 nm compared to VTGCM and VPCM, inducing lower oxygen production. Moreover, the reduced wavelength range of the spectrum used by TUGCM excludes the photoionization process and therefore this farther reduces the production of atomic oxygen, mainly for layers above 10<sup>-3</sup> Pa (Dickinson and Ridley, 1972).

	VPCM	VTGCM	TUGCM
CO <sub>2</sub> Photochemistry	85–210 nm; QE = 1 QE $\leq$ 1 below 85 nm based on photoionization	85–225 nm; QE = 1 QE $\leq$ 1 below 85 nm based on photoionization	100–200 nm; QE = 1 ( $\lambda \geq$ 167 nm), QE = 0.5 ( $\lambda \leq$ 167 nm) no photoionization
EUV spectrum and heating scheme	0.1–800 nm González-Galindo et al. (2005, 2013)	0.1–225 nm Schunk and Nagy (2009)	5–105 nm Torr et al. (1979)
EUV heating efficiency	19.5%	20%	10%
Thermal conductivity coefficients ( $J$ m <sup>−1</sup> s <sup>−1</sup> K <sup>−1</sup> )	$k_o = 7.59 \times 10^{-4} \times T^{0.69}$ $k_{co} = 4.87 \times 10^{-4} \times T^{0.69}$ $k_{co2} = 3.072 \times 10^{-4} \times T^{0.69}$ from Banks and Kockarts (1973)	$k_o = 7.59 \times 10^{-4} \times T^{0.69}$ $k_{co} = 4.87 \times 10^{-4} \times T^{0.69}$ $k_{co2} = 3.072 \times 10^{-4} \times T^{0.69}$ from Banks and Kockarts (1973)	O from Banks and Kockarts (1973) and others species from Chapman and Cowling (1970) $k_{co} = 3.769 \times 10^{-4} \times T^{0.734}$ $k_{co2} = 5.18 \times 10^{-5} \times T^{0.9333}$
Radiative cooling Scheme	Simplified non-LTE model developed for Mars PCM (González-Galindo et al., 2013)	Parametric equations that reproduce the cooling deviation from the reference cooling (Bougher et al., 1986). Two different references are used for day and night (from Roldán et al., 2000).	Parametric equations that reproduce the cooling deviation from the reference cooling (Bougher et al., 1986). Two different references are used for day and night (from Dickinson and Bougher, 1986).
Quenching rate CO <sub>2</sub> -O (cm <sup>3</sup> /s)	$5 \times 10^{-12}$	$3 \times 10^{-12}$	$3 \times 10^{-12}$
NIR heating scheme	Parametric equations that mimic the heating rate of a full line-by-line non-LTE model (Roldán et al., 2000), tuned to reproduce VEx data (Gilli et al., 2017; Martinez et al., 2023).	Offline simulated look-up tables using Roldán et al. (2000) rates.	LTE computed, then scaled to match Roldán et al. (2000)
GW / Rayleigh friction scheme	non-orographic gravity wave Earth GCM-based scheme (Lott et al., 2012; Lott and Guez, 2013; Martinez et al., 2023)	Rayleigh friction tuned to match PVO	Medvedev and Klaassen (2000) scheme with drag efficiency = 0.1

Table 2: Summary of the main physical processes of the thermosphere and key rates for each GCM. QE: Quantum efficiency.

### 2.1.2. EUV spectrum reference and EUV heating parameter

EUV-UV radiation is the main source of heating in the upper thermosphere, which varies with solar activity. The air molecules will absorb this radiation, and a fraction of it will be converted into kinetic energy, resulting in heating. Traditionally, the heating efficiency is defined as the fraction of solar energy absorbed at a given altitude which appears locally as heat. In the case of our nominal models, this efficiency is parameterized with the EUV heating efficiency factor, corresponding to 10% for TUGCM, 20% for VTGCM and 19.5% for VPCM.

In parallel with EUV heating efficiency factor, the solar spectrum used will influence the heating rate. In fact, EUV-UV radiation is highly variable, which can lead to significant differences in the heating rate depending on the reference used. The effects of this variability will be discussed in Section 3 and 3.3, while the model references are presented here:

- For TUGCM, the solar flux model and the absorption cross section follows Torr et al. (1979) and covers from 5 to 105 nm.
- The VTGCM solar flux spectrum (0.1-225.0 nm) with 75-wavelength intervals is presently utilized based upon the Solomon solar flux model commonly used in terrestrial thermospheric general circulation model simulations (e.g. Roble et al., 1988; Richmond et al., 1992; Ridley et al., 2006). Solar EUV fluxes are provided by the EUVAC proxy model (Richards et al., 1994). These solar fluxes are extended below 5 nm (soft X-rays) as described in Solomon and Qian (2005). Similarly, far ultraviolet (FUV) irradiances are provided by the Woods and Rottman (2002) model. Cross sections (and yields) for EUV bins are adopted (partially) from Schunk and Nagy (2009). For the present application, daily F10.7 and 81 day averaged F10.7A indices are set equal in order to generate reference fluxes for typical solar conditions found at F10.7 centimeter indices of 200, 130, and 70. These indices are generally consistent with solar maximum (SMAX), solar moderate (SMED), and solar minimum (SMIN) conditions, respectively. Lastly, the solar fluxes are scaled to the Venus-Sun distance by applying a 1.914 factor.
- VPCM uses a spectrum ranging from 0.1 to 800 nm, but instead of using a solar radiation spectrum, it uses a spectrum of the photoabsorption rate of each species at the top of the atmosphere. VPCM calculates the photoabsorption coefficient of each part of the spectrum

as a function of solar activity (E10.7) with a polynomial fit, based on SOLAR2000 modeling data (Tobiska et al., 2000). Each part is then summed to obtain the total photoabsorption coefficient, as presented in González-Galindo et al. (2005, 2013). This method is expected to be less dependent on the spectral observation variability because it is based on a large number of photoabsorption estimates.

Note that spectrum above 225 nm has only a minor impact on the thermospheric Venusian EUV heating since the main absorbents above 225 nm (e.g. O<sub>3</sub> or H<sub>2</sub>O<sub>2</sub>) have abundances 10 orders of magnitude lower than CO<sub>2</sub> (González-Galindo et al., 2005, 2013).

### 2.1.3. *Thermal Conduction*

Thermal Conduction is the most efficient and main physical process for cooling the upper thermosphere, above 160 km for Venus. On the dayside, this phenomenon transports heat to lower altitudes, where cooling by 15  $\mu\text{m}$  radiation of CO<sub>2</sub> is more efficient, balancing together the EUV-UV heating in the thermosphere. This heat transport will therefore depend on the vertical variation of the thermal structure and the composition. This process is governed by the following equation:

$$\frac{dT}{dt} = \frac{1}{C_p \times \rho} \times \frac{d(k_c \frac{dT}{dz})}{dz} \quad (1)$$

where T is the temperature (K),  $\rho$  the mass density ( $\text{kg m}^{-3}$ ),  $C_p$  the specific heat ( $\text{J kg}^{-1} \text{K}^{-1}$ ) and  $k_c = A \times T^s$  is the thermal conduction coefficient ( $\text{J m}^{-1} \text{s}^{-1} \text{K}^{-1}$ ), with a number density weighted average of the individual species thermal conductivities. The individual specific heat used by each GCM are the same.

VPCM and VTGCM use a similar thermal conductivity coefficient for O, CO, CO<sub>2</sub> and N<sub>2</sub>, and are from the mixed gas prescription of Banks and Kockarts (1973) (where  $s = 0.69$ ). The average molecular coefficient of thermal conductivity of the environment is calculated from the thermal conductivity of CO, CO<sub>2</sub> and O in Hoshino et al. (2012). VPCM and TUGCM have the same formula for O and similar for CO. However, the thermal conductivity of CO<sub>2</sub> is on average 30-40% lower in TUGCM ( $5.18 \times 10^{-5} \times T^{0.9333} \text{ J m}^{-1} \text{s}^{-1} \text{K}^{-1}$ ; Chapman and Cowling, 1970) than in VPCM ( $3.072 \times 10^{-4} \times T^{0.69} \text{ J m}^{-1} \text{s}^{-1} \text{K}^{-1}$ ; Banks and Kockarts, 1973) for  $T \leq 300$  K, which will reduce the efficiency of heat transport by conduction.

#### 2.1.4. *Radiative cooling*

Below 160 km altitude, radiation is the most efficient cooling process, primarily through 15  $\mu\text{m}$  emission of CO<sub>2</sub> bands, which occurs under Non Local Thermodynamical Equilibrium (NLTE) conditions. CO<sub>2</sub> 15  $\mu\text{m}$  emission is known to be enhanced by collisions with O-atoms, providing increased cooling in NLTE regions of the upper atmosphere (see Bouger and Borucki (1994) and Kasprzak et al. (1997)). Yet, the main collisional relaxation rate is not well known with uncertainties of the order of a factor of 2. While laboratory measurements are in the range of 1.5 to  $2 \times 10^{-12}\text{cm}^3\text{s}^{-1}$  at 300 K, the values derived from the Earth's atmosphere observations are close to  $6 \times 10^{-12}\text{cm}^3\text{s}^{-1}$  (see García-Comas et al. (2008) and López-Puertas et al. (2024) for discussion).

The values adopted for typical benchmark simulations are  $3 \times 10^{-12}\text{cm}^3\text{s}^{-1}$  for VTGCM and TUGCM (e.g. a "median" value commonly used in terrestrial atmospheric models), and  $5 \times 10^{-12}\text{cm}^3\text{s}^{-1}$  for VPCM (e.g. within the brackets of the experimental and observational values), respectively.

- TUGCM and VTGCM follow the same parameterization scheme based on Bouger et al. (1986) to simulate the radiative cooling. This consists in calculating approximate thermal infrared cooling using global mean dayside and nightside reference cooling profiles plus a NLTE cool-to-space formulation for deviations from those references. For a given temperature and composition profile, CO<sub>2</sub> NLTE cooling rates were taken from line-by-line radiative transfer model calculations by Roldán et al. (2000) and by Dickinson and Bouger (1986) in VTGCM and TUGCM, respectively. Then, total cooling rates for the simulated temperatures and species abundances are calculated interactively from these rates based upon a nonlinear temperature parameterization scheme described in Bouger et al. (1986).
- VPCM follows a different strategy, similar to that developed in González-Galindo et al. (2013) for the Mars PCM, with a simplified non-LTE model taking into account the 5 strongest ro-vibrational bands of CO<sub>2</sub> (instead of 92 for the complete non-LTE model) and allows for a variable abundance of atomic oxygen. The details of the implementation of the scheme into the VPCM are in Gilli et al. (2017).

### 2.1.5. *NIR heating*

The absorption of solar radiation in the CO<sub>2</sub> IR bands significantly affects the thermal structure of Venus' atmosphere above 90-100 km. In the thermosphere, this process occurs mainly under NLTE conditions, while below 90 km it is generally assumed to follow local thermodynamic equilibrium (LTE). The most comprehensive study of the NIR heating rate was carried out by Roldán et al. (2000) using a line-by-line NLTE full model for Venus. This work is still the main reference for thermospheric modeling of Venus. In our study, all three GCMs are based on Roldán et al. (2000) for their NIR heating rates, though each model implements it differently.

- In the VTGCM, the near-infrared heating term is incorporated using offline simulated look-up tables, following Roldán et al. (2000) rates.
- In the TUGCM, the LTE near-infrared heating rate is calculated at every grid point. To estimate the non-LTE NIR heating rate, the model multiplies the LTE values by a scaling factor. This factor is chosen so that the global mean LTE heating rate matches the reference NIR heating rate provided by Roldán et al. (2000).
- VPCM recently updated its NIR heating rate calculation in Martinez et al. (2023). Building on the results of Roldán et al. (2000) and using a parameterization originally developed for the Mars PCM (Forget et al., 1999), the authors adjusted each heating band from Roldán et al. (2000) to reproduce its variability with pressure and solar zenith angle (SZA, see details in Appendix A in Martinez et al., 2023).

### 2.2. *Gravity waves or Rayleigh friction*

The observations of Venus' middle atmosphere between 40 and 70 km altitude, as well as observations of the mesosphere and thermosphere above 90 km, revealed the presence of wave structures (Kasprzak et al., 1988; Garcia et al., 2009; Peralta et al., 2008). These gravity waves can be generated by several processes, such as convection within cloud level (50 to 60 km), or the shear instability around 80 km or around the polar vortex. It was then hypothesized that GW generated in the Venusian convective cloud layer could carry the momentum that drives the retrograde superrotation zonal regime. Due to the absence of continuous observations, the characteristics of these waves are poorly constrained, leaving significant uncertainties in their modeling.

Bouger et al. (1988) were the first to investigate the effect of GW drags, assuming Rayleigh friction, and suggesting that this wave drag should decelerate thermospheric winds in the thermosphere. The effect of these GW has important consequences for the dynamics of Venus: by decelerating the zonal wind, the day-to-night transport would be also reduced, producing less nightside adiabatic compressional heating (i.e. the dominant source of nightside heating, Schubert et al., 1980; Bouger et al., 1988). This effect was also simulated in Martinez et al. (2023), where the inclusion of a non-orographic GW scheme allowed to reproduce nightside temperatures close to those observed by Pioneer Venus. Different models have therefore developed strategies to take into account the dynamic effect of these waves on Venus' circulation.

- For VPCM, the impact on the Venusian atmospheric circulation of the non-orographic small-scale GW generated by convection in the cloud layer is based on the formalism developed for the Earth GCM and fully described in Lott et al. (2012) and Lott and Guez (2013). The parameters and their values used are presented in more detail in Gilli et al. (2021) and Martinez et al. (2023).
- TUGCM uses the parameterization developed by Medvedev and Klaassen (2000) also based on the GW spectral evolution and saturation theory described in Medvedev and Klaassen (1995). However, following the recommendations of Alexander et al. (1992), TUGCM applies a wave drag efficiency factor of 0.1 to reduce the drag intensity in the parameterization scheme. This choice reflects the assumption that, if wave activity is intermittent, the time-averaged wave drag force should be approximately one-tenth of the instantaneous force (Hoshino et al., 2013).
- In the VTGCM, the Rayleigh friction is adopted to mimic wave-drag effects on the mean flow; this drag is thought to result from GW momentum deposition. The parameters (described in Brecht et al., 2011) are based upon observations with a specified exponential profile dependent on  $\cos(\text{latitude})$  which is empirically found to best match PVO and VEX observations. As in Brecht et al. (2021), this paper uses Rayleigh friction to provide an overall zonally symmetric "deceleration" of the wind above  $\sim 110$  km. This Rayleigh friction is applied on zonal and meridional winds.

The diurnal thermospheric structure of the gravity wave drag predicted by each model for equatorial latitude is shown in Figure S.1 in the supplementary material.

### 3. Results

Starting from their respective initial states, the models were run for one solar Venusian day to allow for temporal averaging over this period. This duration is sufficient for the purposes of this study, as the timescales governing the upper atmosphere (particularly in the mesosphere and thermosphere) are much shorter than those below the cloud layer (typically less than a few Earth days at 110 km, and even shorter at higher altitudes). In this section, pressure is used as the vertical coordinate, as heating and cooling processes primarily depend on pressure rather than geometric altitude, focusing on regions above approximately 85 km (or  $\sim 100$  Pa).

#### 3.1. *Thermal and Dynamical structure of benchmark simulations*

##### 3.1.1. *Thermal structure*

Figure 1 compares the diurnal thermospheric temperature profiles at equatorial latitudes ( $30^{\circ}\text{S}$ – $30^{\circ}\text{N}$ ) predicted by three models (VPCM, VTGCM and TUGCM) from 100 Pa up to  $1 \times 10^{-6}$  Pa under both high (E10.7 = 200 s.f.u) and low (E10.7 = 70 s.f.u) solar activity. All models show a local temperature maximum around noon in the mid-thermosphere, with VPCM and TUGCM peaking around 225 K and VTGCM around 245 K. However, TUGCM's peak is shifted to lower pressure ( $\sim 5 \times 10^{-3}$  Pa) compared to  $\sim 0.1$  Pa for the others.

- **Dayside Thermosphere (Local time [LT]=[09-15H])**

On the dayside, the mean upper thermospheric temperatures range between 315–340 K (for  $P \leq 2 \times 10^{-5}$  Pa). Under low solar activity, dayside upper thermospheric temperatures drop to 210 K (TUGCM), 248 K (VTGCM), and 264 K (VPCM). For layers below  $2 \times 10^{-3}$  Pa temperature fields are largely unaffected by solar activity, as this region is dominated by NIR heating (varying with the solar cycle as low as 0.05% at wavelengths in the visible and infrared ranges; Woods et al., 2018) and by 15  $\mu\text{m}$  radiative cooling.

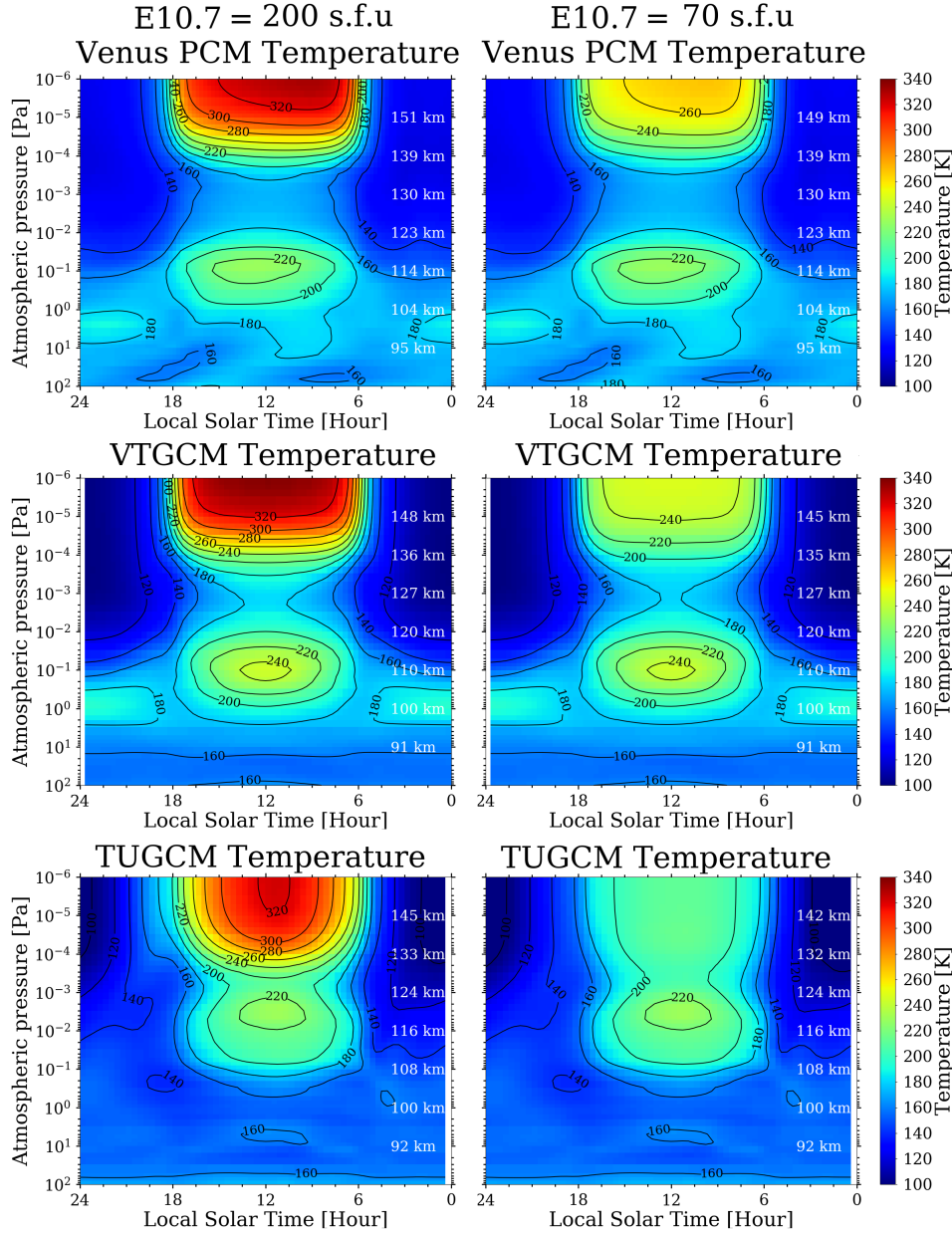


Figure 1: Diurnal structure of the temperatures for equatorial latitude ( $30^{\circ}\text{S}$ - $30^{\circ}\text{N}$ ) for Venus PCM (top), VTGCM (middle) and TUGCM (bottom) at high solar activity ( $\text{E10.7} = 200 \text{ s.f.u}$ ; leftside) and at low solar activity ( $\text{E10.7} = 70 \text{ s.f.u}$ ; rightside). The approximate altitude of each model for each solar activity is marked in white for pressure levels of  $10, 1, 0.1, 10^{-2}, 10^{-3}, 10^{-4}$  and  $10^{-5} \text{ Pa}$ .

- **Dayside Mesopause Characteristics**

The mesopause is the boundary between the mesosphere and the thermosphere, and is characterized by a strong temperature inversion, with a minimum temperature. On Venus, the mesopause (e.g. base of the thermosphere) is located in the altitude range between 90 and 130 km, depending on the local time, latitude and solar conditions (Schubert et al., 2007). The models also differ in mesopause characteristics. For equatorial latitudes, VPCM and VTGCM place the mesopause around  $2 \times 10^{-3}$  Pa while TUGCM locates it higher ( $6-7 \times 10^{-4}$  Pa). These differences arise mainly from variations in NIR heating and 15  $\mu\text{m}$  cooling rates (see Fig. 2).

- **Nightside Thermosphere (Local time [LT]=[21-03H])**

On the nightside (for  $P \leq 2 \times 10^{-5}$  Pa), VTGCM and TUGCM simulate cooler temperatures ( $\sim 100-105$  K) compared to VPCM (120–125 K). Under low solar activity nightside values remain unchanged. Both VTGCM and VPCM simulate a warm layer around 1–3 Pa (185–195 K), attributed to adiabatic heating driven by SS–AS circulation, consistent with past observations (see section 4.1). Since the NIR heating in TUGCM is weaker than in VTGCM and VPCM for atmospheric layers below  $10^{-2}$  Pa, the colder nightside temperatures observed below  $10^{-1}$  Pa are interpreted as a result of reduced day-to-night winds at these altitudes. This reduction in wind is partly driven by cooler dayside temperatures, which lead to weaker adiabatic heating.

- **Heating and cooling below 1 Pa**

For layers below 1 Pa (see Fig. 2), TUGCM shows significantly cooler temperatures due to a NIR heating rate nearly half that of VPCM. VTGCM's NIR heating is comparable to VPCM, but its stronger 15  $\mu\text{m}$  cooling contributes to lower temperatures overall.

### 3.1.2. *Dynamical structure*

Figure 3 shows the diurnal thermospheric zonal winds at equatorial latitudes ( $30^{\circ}\text{S}$ – $30^{\circ}\text{N}$ ) predicted by each model, from 100 Pa up to  $1 \times 10^{-6}$  Pa under high ( $E10.7 = 200$  s.f.u) and low ( $E10.7 = 70$  s.f.u) solar activity. See Figure S.2, S.3 and S.4 in the supplementary material for vertical and meridional wind structure. Wind intensity at the terminators is driven by the day–night temperature gradient and modified by gravity wave drag or

Latitude: 30S-30N, 12h LT

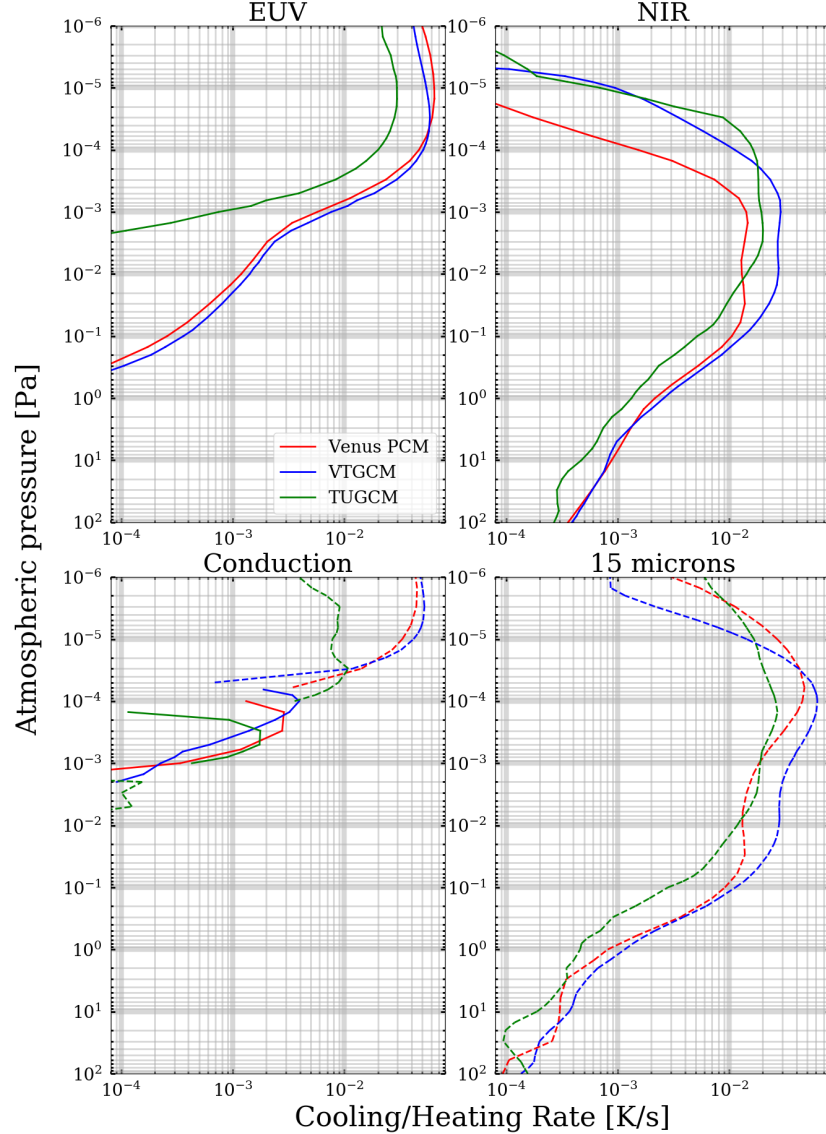


Figure 2: Vertical profile of the EUV heating (top, leftside), NIR heating (top, rightside), conduction heating/cooling (bottom, leftside) and radiative cooling (bottom rightside) rates [K/s] at high solar activity ( $E10.7 = 200$  s.f.u) obtained for equatorial latitude ( $30^{\circ}\text{S}-30^{\circ}\text{N}$ ) at noon for VPCM, VTGCM and TUGCM. The cooling/heating processes have negative/positive value. Cooling processes are plotted with dashed lines. Blue, red and green lines correspond to VTGCM, VPCM and TUGCM.

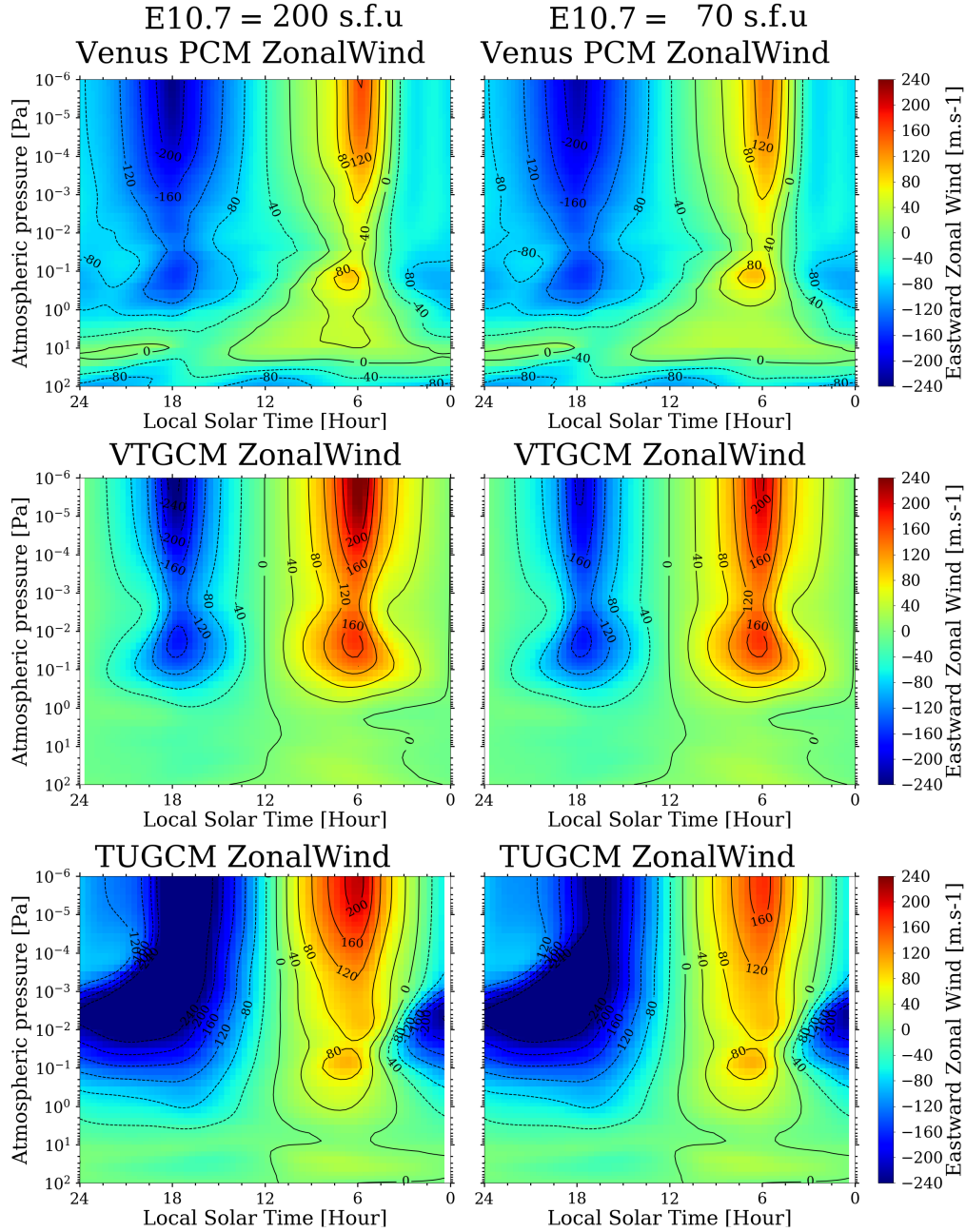


Figure 3: Diurnal structure of the zonal wind for equatorial latitude ( $30^{\circ}\text{S}$ - $30^{\circ}\text{N}$ ) for Venus PCM (top), VTGCM (middle) and TUGCM (bottom) at high solar activity ( $E10.7 = 200$  s.f.u; leftside) and at low solar activity ( $E10.7 = 70$  s.f.u; rightside).

Rayleigh friction, which reduce wind amplitude. For layers below  $3 \times 10^{-4}$  Pa, solar activity has little effect on wind structure. Above this level, all models show slightly stronger terminator winds at high solar activity, due to increased temperature gradients (see Fig. 1).

Above 1 Pa, VPCM and TUGCM show wind asymmetries caused by GW drag, which induces stronger braking in the morning sector. In contrast, VTGCM exhibits a more symmetric wind pattern due to uniform Rayleigh friction that scales with wind amplitude. Morning-side wind amplitudes are similar across models, though VPCM is  $\sim 20\%$  weaker than VTGCM and TUGCM at  $10^{-6}$  Pa. On the evening side, TUGCM predicts much stronger winds (-360 m/s) compared to VPCM and VTGCM (-200 m/s), due to a lower drag coefficient in that region.

Below 30 Pa, VPCM maintains a super-rotation regime, while VTGCM and TUGCM appear in a transitional state between super-rotation and thermospheric flow. The development of stronger zonal winds in this region is inhibited by the proximity of the VTGCM and TUGCM lower boundaries, located at 4400 Pa ( $\sim 70$  km) and 356 Pa ( $\sim 80$  km), respectively. For example, at 200 Pa, TUGCM reaches -20 m/s and VTGCM -50 m/s compared to -80 m/s for VPCM. Different lower boundary conditions have an impact on the horizontal wind structure. Brecht et al. (2021) demonstrated that updating the lower boundary conditions of VTGCM (from uniform to varying) only impacts the temperature and the winds up to 80 km. Ponder et al. (2024) also studied the sensitivity of horizontal winds of their GCM (V-GITM) to different conditions of lower boundary at 70 km (e.g. zonal wind of 0, -50 and -100 m/s) showing that the largest differences occur for layers below 105 km.

### 3.2. Neutral Composition: $CO_2$ , $N_2$ , $CO$ , $O$

For this comparison exercise, we focus only on the most abundant neutral species in the thermosphere, which are  $CO_2$ ,  $N_2$ ,  $CO$  and  $O$ , considering that minor species do not have a considerable impact on the temperature profile in the pressure range studied. As mentioned in Section 2, the three models studied in this article have two different compositional backgrounds in the deep atmosphere. VPCM and VTGCM have 96.5% of  $CO_2$  and 3.5% of  $N_2$ , while TUGCM has 100% of  $CO_2$ . These composition differences are clearly visible in Figure 4, which shows the vertical pressure profile of the dayside thermosphere composition. TUGCM has a vertical profile of  $CO$  and  $O$  that differs greatly from VTGCM and VPCM with an atomic oxygen density

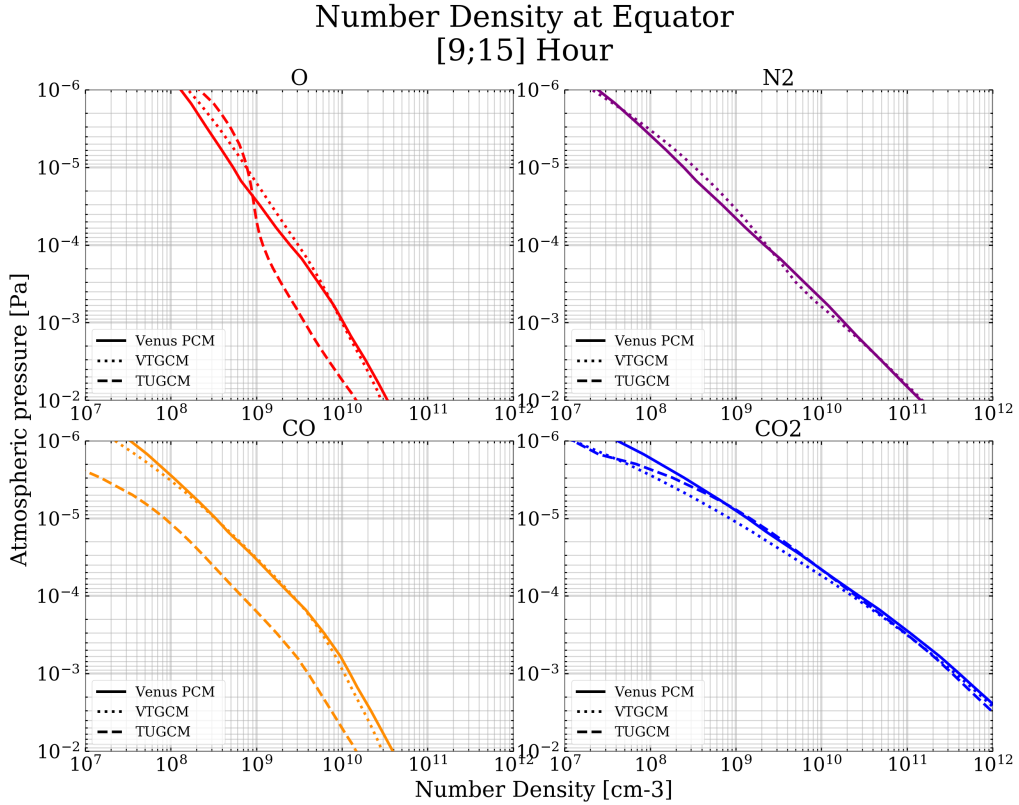


Figure 4: Vertical profile of the dayside thermosphere composition ( $\text{CO}_2$  in blue,  $\text{N}_2$  in purple, CO in orange and O in red) around the equator ( $30^\circ\text{S}$ - $30^\circ\text{N}$ ) for each GCM at high solar activity ( $\text{E}10.7 = 200$  s.f.u). Solid lines correspond to VPCM. Dashed lines correspond to TUGCM. Dotted lines correspond to VTGCM. Note that TUGCM does not include  $\text{N}_2$ .

more than 2 times lower for layers below  $10^{-4}$  Pa, and higher for layers above  $2 \times 10^{-5}$  Pa. For layers below  $10^{-4}$  Pa, VTGCM and VPCM have a similar vertical profile. For layers above  $10^{-4}$  Pa, the decay of  $\text{CO}_2$  with pressure is greater in VTGCM than in TUGCM and VPCM. The atomic oxygen number density modeled by VTGCM is also between 20 and 50% more dense than VPCM.

On the dayside, the production of atomic oxygen due to photoabsorption is comparable to the loss rate from vertical advection in atmospheric layers above 1 Pa and below  $2 \times 10^{-4}$  Pa (Hoshino, 2011). For layers above 0.1 Pa, atomic oxygen losses by chemistry are negligible compared to chemical

production (Brecht et al., 2011) and for layers above  $10^{-4}$  Pa, molecular diffusion becomes the dominant transport process. As mentioned in Section 2.1.1, TUGCM does not take into account the solar spectrum for photochemistry below 100 nm and has a photodissociative quantum efficiency 2 times smaller than VTGCM and VPCM. As a result, the difference between TUGCM and VTGCM/VPCM in CO and O production increases with altitude, from more than a factor of 2 at 0.1 Pa to more than 8 at  $10^{-6}$  Pa. This helps explain the lower O and CO densities simulated by TUGCM compared to VPCM and VTGCM within the  $0.1\text{--}10^{-4}$  Pa pressure range. Thus, the difference in atomic oxygen density between TUGCM and VTGCM/VPCM for layers above  $10^{-4}$  Pa can only be explained by transport processes. Our best guess is that this is due to the molecular diffusion scheme, since only O-atoms is concerned, and that this deviation begins when molecular diffusion becomes the main vertical transport process. Moreover, Hoshino (2011) suggests that the rapid mass separation in TUGCM is caused by molecular diffusion. In the case of the rapid decay of CO<sub>2</sub> in VTGCM, our best guess is that the difference is due to the advection process, linked to the dynamics of VTGCM which takes variable molecular mass into account when calculating transport.

### 3.3. *Impact of variation of EUV heating*

At high solar activity (see blue curves in Figure 2 and solid curves in Figure 5), all three models produce similar shaped EUV heating profiles but with different peak amplitudes and vertical locations. The EUV heating peak reaches 0.03 K/s at  $1.5 \times 10^{-5}$  Pa for TUGCM, 0.065 K/s at the same pressure for VPCM, and 0.058 K/s at  $3 - 4 \times 10^{-5}$  Pa for VTGCM. Note that for layers below  $5 \times 10^{-4}$  Pa TUGCM's EUV heating profile declines more rapidly than in the other two models.

The lower heating rate in TUGCM arises mainly from two factors. First, it uses a lower EUV heating efficiency (10%), compared to 19.5% and 20% for VPCM and VTGCM, respectively. Doubling TUGCM's heating amplitude for  $P \leq 5 \times 10^{-5}$  Pa would bring it in line with the others (see Fig. 2). Second, TUGCM uses a narrower EUV spectral range (5–105 nm from Torr et al., 1979) compared to 0.1–800 nm in VPCM (González-Galindo et al., 2005, 2013; Gilli et al., 2017) and 0.1–225 nm in VTGCM (Brecht, 2011). As shown in Fox (2007), wavelengths above 105 nm penetrate deeper into the atmosphere. Thus, for  $P \geq 1 \times 10^{-4}$  Pa, TUGCM's lower heating rate is largely due to its limited spectral coverage.

For the high solar activity case, the EUV heating rate in VPCM is larger than in VTGCM for layers above  $4 \times 10^{-5}$  Pa, and smaller below. However, the two models are relatively similar for low solar activity (70 s.f.u, see Figure 5). This can be explained by two factors: larger solar spectrum intensity and different spectral variability that favors wavelengths that penetrate deeper into the atmosphere. Moreover, CO<sub>2</sub> absorbs EUV more efficiently than O, so differences in CO<sub>2</sub> abundance can slightly reduce VTGCM's heating compared to VPCM (González-Galindo et al., 2013). Additionally, VTGCM shows a faster decay of CO<sub>2</sub> density with altitude, meaning unit optical depth is reached at higher pressures. VTGCM also uses higher spectral resolution, which can improve the accuracy of vertical absorption profiles and heating rates. However, González-Galindo et al. (2005) showed that the chosen spectral distribution produces similar heating profiles for resolutions between 0.1 and 1 nm. Resolution differences alone do not significantly affect its heating profile.

### 3.3.1. *Solar Cycle effect*

The variation of EUV heating rate with solar activity (from low to high) shows peak increases by a factor of  $\sim 1.7$  for VPCM,  $\sim 2.2$  for VTGCM, and  $\sim 3$  for TUGCM (see Fig.5). These differences arise mainly from the reference spectra used under each solar condition. As discussed in Section 2.1.2, both VTGCM and TUGCM rely on observed or clustered spectra for different solar activity levels. The variability is smaller in VTGCM than in TUGCM, likely because VTGCM uses more recent reference data. Older spectra, such as Torr et al. (1979) used by TUGCM, are known to overestimate photon flux at high activity (Torr and Torr, 1985), which amplifies the solar cycle effect.

In contrast, VPCM employs a different approach: it calculates photoabsorption coefficients for each spectral band as a function of solar activity (E10.7), using polynomial fits from the SOLAR2000 model (Tobiska et al., 2000). These are summed following the method described in González-Galindo et al. (2005, 2013) (see Section 2.1.2). This yields a CO<sub>2</sub> absorption variation of about a factor 1.7 between 70 and 200 s.f.u., consistent with the observed variation in peak heating. However, studies such as Rozelot et al. (2009) indicate that for wavelengths below 90 nm, spectral intensity typically varies by at least a factor of 2 across the solar cycle.

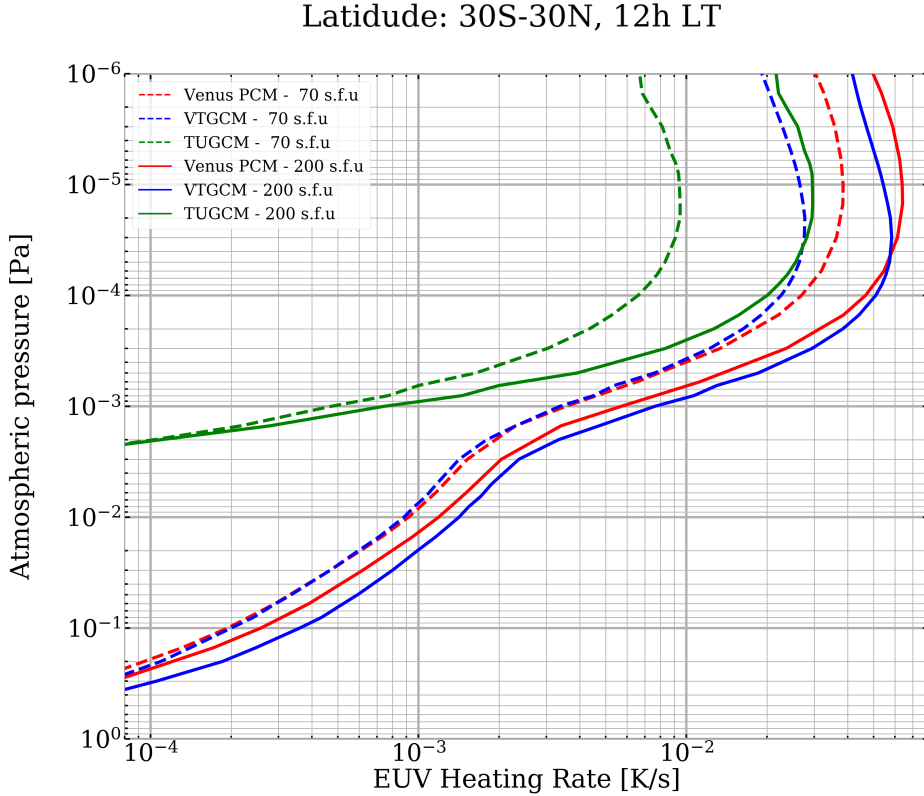


Figure 5: Vertical profile of EUV heating rate obtained at noon for equatorial latitude ( $30^{\circ}\text{S}$ - $30^{\circ}\text{N}$ ) and for different solar activity and for each GCM (Solid line: high solar activity; dashed line: low solar activity; VPCM in red, VTGCM in blue and TUGCM in green).

### 3.4. Impact of different conductivity rates on exospheric temperatures

As discussed in Section 2.1.3, TUGCM uses a lower  $\text{CO}_2$  thermal conductivity coefficient ( $5.18 \times 10^{-5} \times T^{0.9333} \text{ J m}^{-1} \text{ s}^{-1} \text{ K}^{-1}$ ; Chapman and Cowling, 1970) than VPCM and VTGCM ( $3.072 \times 10^{-4} \times T^{0.69} \text{ J m}^{-1} \text{ s}^{-1} \text{ K}^{-1}$ ; Banks and Kockarts, 1973), which reduces the efficiency of heat transport to lower altitude, particularly in the region dominated by  $\text{CO}_2$  NLTE radiative cooling ( $\sim 10^{-3}$  Pa and  $\sim 10^{-5}$  Pa).

We conducted several tests (summarized in table 3) to assess the impact of different conductivities on the model temperature. First, VPCM was run

with a CO<sub>2</sub> conductivity similar to that used in TUGCM (keeping the N<sub>2</sub> in the calculation). At high solar activity, the dayside upper thermosphere temperature increased from 325 K to 340 K. In a second test, VPCM also adopted the CO<sub>2</sub>-O quenching coefficient used in TUGCM ( $3 \times 10^{-12} \text{ cm}^3 \text{s}^{-1}$ ), resulting in a further temperature rise to over 405 K (compared to 375 K in the baseline VPCM setup). For reference, in a TUGCM simulation using the same EUV heating efficiency as VPCM/VTGCM, the dayside temperature exceeds 730 K. This comparison will be discussed further in the next subsection.

Thus, the lower CO<sub>2</sub> thermal conductivity in TUGCM alone cannot account for the large temperature differences observed with VTGCM and VPCM, though it has a minor influence that should not be neglected in future studies. Currently, the significant discrepancy in conduction heating/cooling rates at noon between TUGCM and the other models is most likely due to the method TUGCM uses to calculate thermal conduction, although rapid compositional changes may also contribute.

<i>Simulations at high solar activity</i>	<i>Dayside exospheric temperature</i>
VPCM nominal case	325 K
VTGCM nominal case	338 K
TUGCM nominal case	315 K
VPCM with CO <sub>2</sub> thermal conductivity of TUGCM	340 K
VPCM with quenching rate = $3 \times 10^{-12} \text{ cm}^3 \text{s}^{-1}$	375 K
VPCM with quenching rate = $3 \times 10^{-12} \text{ cm}^3 \text{s}^{-1}$ and CO <sub>2</sub> thermal conductivity of TUGCM	405 K
TUGCM with EUV heating efficiency = 20%	730 K

Table 3: Dayside exospheric temperature for different tests compared with the nominal case described in Table 2, as reference. The values correspond to the simulated temperature during high solar activity (EUV index of 200 s.f.u.) averaged from  $2 \times 10^{-6}$  Pa up to the top level of each model, between 9-15 LT and around the equator (30°S-30°N).

### 3.5. *Impact of Radiative cooling parameterization*

Radiative cooling is highly sensitive to the parameterization implemented in simulations. Since our three models use different schemes and reference temperature profiles (see Section 2.1.4), their radiative cooling efficiency varies accordingly.

VTGCM and TUGCM share the same thermal cooling formulation and quenching rate, enabling a direct comparison based on reference cooling rates

and atomic oxygen densities. Although both models follow the Bouger et al. (1986) scheme, VTGCM uses updated reference 15- $\mu\text{m}$  cooling rates from Roldán et al. (2000), while TUGCM uses older values from Dickinson and Bouger (1986). This scheme depends on the oxygen density versus  $\text{CO}_2$  density for layers above than  $10^{-2}$  Pa (in the non-LTE region). A test using Dickinson and Bouger (1986) formulation with each model's atomic oxygen density shows that TUGCM's cooling is 10–35% weaker than VTGCM between  $10^{-3}$  and  $5 \times 10^{-6}$  Pa. For layers above this range, differences in atomic oxygen density become negligible.

At the 15  $\mu\text{m}$  cooling peak around  $1 \times 10^{-4}$  Pa, TUGCM's cooling rate is about 2.2 times lower than VTGCM, despite having a 20 K higher temperature at the same pressure, highlighting the dominant role of reference cooling rates. For layers above  $10^{-5}$  Pa, TUGCM shows larger cooling than VTGCM. Overall, these findings suggest that differences in reference rates are the primary source of variation. A more detailed comparison would require consistent temperature, pressure, and  $\text{O}/\text{CO}_2$  density inputs across models.

As explained in Section 2.1.4, VPCM uses a different non-LTE scheme, similar to González-Galindo et al. (2013), simplifying  $\text{CO}_2$  band treatment to five dominant bands and allowing variable atomic oxygen. Lowering the quenching coefficient from  $5 \times 10^{-12}$  to  $3 \times 10^{-12} \text{ cm}^3\text{s}^{-1}$  raises exospheric temperatures by 50 K on the dayside, making VPCM's cooling less efficient than VTGCM. For layers above  $10^{-4}$  Pa, this may also reflect VPCM's higher heating rates and an underestimation of atomic oxygen by 20–50% (see Fig. 4).

For pressures  $\geq 10^{-4}$  Pa, differences between VPCM and VTGCM/TUGCM come from their use of outdated VIRA or VTS3 reference profiles, which underestimate temperatures near 120–150 km compared to VEx observations (Limaye et al., 2017; Gilli et al., 2017, 2021). This likely inflates the cooling efficiency in VTGCM/TUGCM. VPCM's lower cooling efficiency for layers below  $10^{-3}$  Pa may also result from neglecting minor non-LTE  $\text{CO}_2$  bands included in VTGCM and TUGCM via the Roldán et al. (2000) reference. However, these bands contribute less than the five primary ones already modeled.

When TUGCM assumes 20% EUV heating efficiency, daytime temperatures exceed 730 K, compared to 338 K for VTGCM and 315 K for TUGCM at 10% efficiency. This sharp increase results from both doubled heating and reduced cooling for layers above  $5 \times 10^{-4}$  Pa, driven by a 3–5 times drop in

atomic oxygen density. This variation, caused by the change in EUV heating efficiency, suggests that, for layers above  $1 \times 10^{-5}$  Pa, the lower TUGCM temperature compared to VTGCM and VPCM visible in Figure 1 is the result of a lower EUV heating efficiency compared with typical values used for Venus.

Overall, these models highlight the critical role of atomic oxygen abundance in regulating thermospheric temperatures.

### 3.6. *Variability of NIR heating*

Figure 2 highlights notable differences in NIR heating intensity and its variation with altitude. These differences are mainly due to the method used to take into account non-LTE effects following the line-by-line radiative transfer model in Roldán et al. (2000), as explained in Section 2.1.5. All three models assume the NIR heating rate is independent of the solar cycle, since the NIR spectrum itself does not vary significantly with solar activity (Woods et al., 2018), and there is no reference model for low solar activity.

Roldán et al. (2000) performed a sensitivity analysis of the impact of O abundance on the NIR heating rates. They showed that reduced atomic oxygen abundance decreases NIR heating in the 2.7 and 4.3  $\mu\text{m}$  bands above 120–125 km. However, the variability of NIR heating rates due to O abundance changes is not taken into account by any models. Therefore, since the reference heating rates in the models are taken from Roldán et al. (2000) for a fixed atmospheric composition, we had to overestimate the heating efficiency to compensate for the deficit of atomic oxygen above 130 km in all models. In contrast, the 15  $\mu\text{m}$  cooling efficiency is evaluated internally and uses the modelled atomic oxygen abundance, as detailed in Section 2.1.4.

In the absence of observations of atomic oxygen during low solar activity, it is reasonable to expect some solar cycle-related variability in NIR heating, due to changes in atomic oxygen production above 125 km. The lack of observations hinders our ability to constrain this variability in models.

### 3.7. *Vertical variability of the pressure-altitude level*

In previous sections, results were shown using vertical pressure scales. Since most atmospheric processes depend primarily on pressure, comparing models in pressure coordinates is more appropriate than using altitude. Differences in temperature and composition among models significantly affect

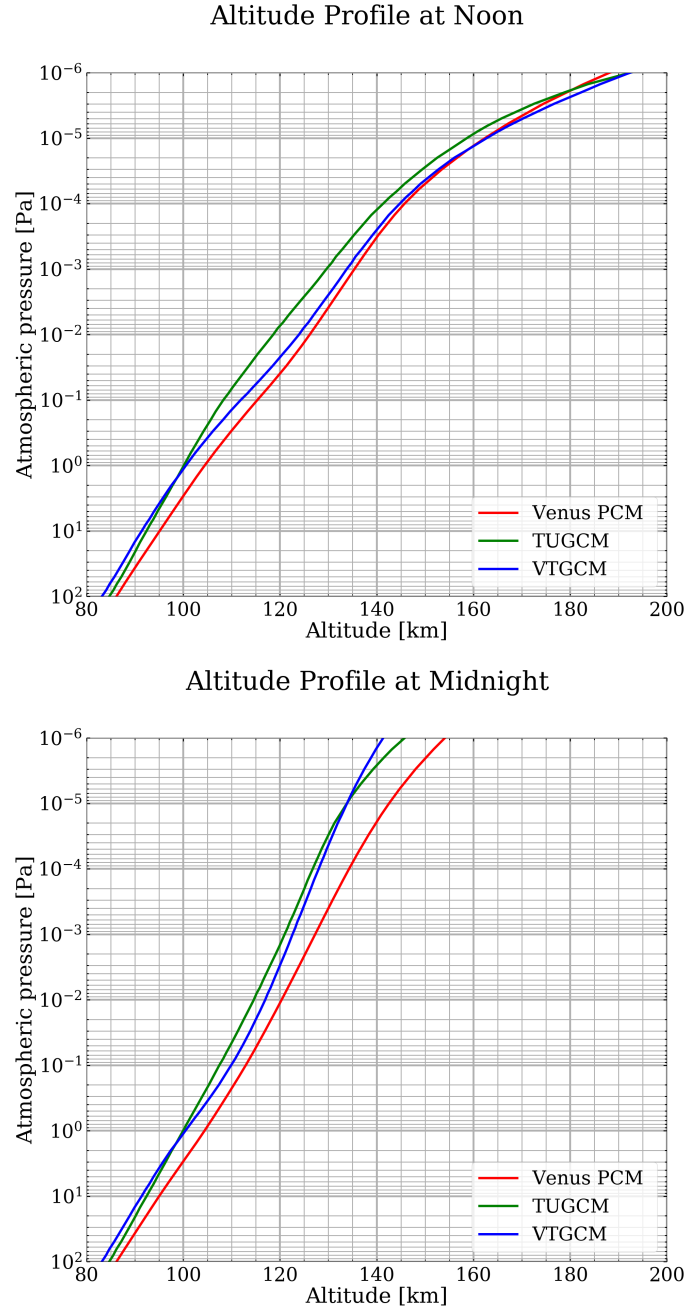


Figure 6: Vertical profile of altitude at noon (top) and at midnight (bottom) for each GCM at high solar activity ( $E_{10.7} = 200$  s.f.u; VPCM in red, VTGCM in blue and TUGCM in green).

altitude estimates. From the hydrostatic equation, the relation between pressure and altitude is:  $(z-z_0) = H \times \log\left(\frac{p_0}{p}\right)$  where  $H = \frac{k_B \times T}{m_{mol} \times g}$  is the scale height.  $z$  is the altitude,  $z_0$  and  $p_0$  are the reference altitude (in meters) and pressure (in Pa), respectively,  $T$  is the temperature,  $g$  is the gravitational acceleration (in  $\text{m/s}^2$ ),  $m_{mol}$  is the mean molecular mass of the atmosphere (in  $\text{g/mol}$ ) and  $k_B$  is the Boltzmann constant. Thus, altitude differences between two pressure levels depend on the ratio  $T/m_{mol}$ , the higher this ratio, the greater the altitude gap.

Figure 6 shows the vertical altitude profile at midnight and noon for each GCM under high solar activity. Notable differences arise due to variations in composition and temperature. At  $\sim 100$  Pa, VPCM is  $\sim 3$  km higher than VTGCM and  $\sim 1.5$  km higher than TUGCM. Although VPCM and VTGCM share similar lower atmospheric compositions, VTGCM's faster  $\text{CO}_2$  decline for layers above  $10^{-4}$  Pa reduces mean molecular mass, increasing altitude differences. Additionally, VTGCM is warmer than VPCM for layers above 1 Pa, widening the noon altitude gap from  $-3$  km at  $10^2$  Pa to  $+4$  km at  $10^{-6}$  Pa. For pressure between 100 and 1 Pa, the gap is larger, caused by the lower temperature of VTGCM.

TUGCM shows lower altitudes overall due to its higher molecular weight (44 g/mol, from the absence of  $\text{N}_2$ ) and lower temperatures. However, for layers above  $10^{-2}$  Pa, the rapid increase in O abundance and its higher temperature reverse this trend, reducing this gap with VPCM from  $-5$  km at  $10^{-4}$  Pa to  $+4$  km at  $10^{-6}$  Pa.

On the nightside, the cooler temperatures in VTGCM and TUGCM compared to VPCM result in a steeper pressure decrease with altitude, reversing the trend seen during the day.

#### 4. Benchmark GCMs *vs* Observations

In this section we will compare nominal GCMs simulations with temperature and composition measurements of the upper atmosphere of Venus. Regarding the exospheric temperatures, the values used here are reconstructed from atomic oxygen data measured by Neutral Mass Spectrometer on board Pioneer Venus Orbiter (PV-ONMS), using the method of Mahajan et al. (1990), as detailed in Martinez et al. (2023). No direct measurements of exospheric temperatures are available. Only data above 170 km on the dayside and 150 km on the nightside were used (as in Martinez et al., 2023) to minimize temperature gradient effects. Exospheric temperatures were derived

by fitting atomic oxygen number densities under the assumption of hydrostatic equilibrium:  $N(z)=N(z_0) \times \exp\left(\frac{-(z-z_0)}{H}\right)$  where  $H=\frac{k_B \times T_{exo}}{m_o \times g(z)}$  is the scale height.  $N(z)$  is the number density at  $z$ ,  $z$  is the altitude,  $z_0$  is the reference altitude (average altitude of the orbit),  $g(z)$  is the gravitational acceleration with  $g(0) = 8.87 \text{ m/s}^2$ ,  $T_{exo}$  is the exospheric temperature (which is constant from the middle thermosphere upward) and  $m_o$  is the molar mass of atomic oxygen (16 amu). Atomic oxygen was selected to determine  $T_{exo}$  because it is among the most abundant species in Venus' upper atmosphere and has been used as a reference in studies since the PV mission.

The most detailed dataset of the neutral composition of the thermosphere above 140 km were made by PV-ONMS between 1978 and 1982 during a period of high solar activity ( $\sim 180\text{--}250$  s.f.u; Niemann et al., 1980). PV-ONMS measured the number densities of He, N, O, CO, N<sub>2</sub> and CO<sub>2</sub> near the equator (centered on 16°N), over nearly three diurnal Venusian cycles, from altitudes of 140–150 km up to 250 km (300 km for He). Here, we use the same data and the same protocol than in Martinez et al. (2023), applying the sensitivity correction factors (k-values) from Keating et al. (1985) to the PV-ONMS measurements:  $\times 1.83$  for the CO<sub>2</sub> and  $\times 1.58$  for the others species. These corrections align NMS measurements with the PV-Orbiter Atmospheric Drag (OAD; Hedin et al., 1983; Keating et al., 1985) dataset.

#### 4.1. Temperature

##### 4.1.1. Diurnal temperature at the upper thermosphere

Figure 7 shows the diurnal variation of the Venusian exospheric temperature derived from the atomic oxygen height scale around  $200\pm 15$  s.f.u. The nightside temperature is  $116\pm 11$  K ("cryosphere") on average, while the day-side temperature is  $287\pm 11$  K according to the PV-ONMS data around 200 s.f.u, with a rapid hourly variation at 6 and 18 LT. These values are in excellent agreement with previous estimates of Niemann et al. (1980) (285 K on dayside and 110 K on nightside).

Significant differences are observed between the diurnal variation of exospheric temperature predicted by models and that reconstructed from observations. On the day-side, all the models overestimate PV-ONMS temperature ( $287\pm 11$  K). Model averages between 9 and 15 LT are with 325 K for VPCM, 338 K for VTGCM and 315 K for TUGCM. On the nightside, all models fall within the observed variability range ( $116\pm 11$  K), with VPCM at 125 K and VTGCM/TUGCM around 105 K, though the latter are near the lower limit. Note that these values are also consistent with SPICAV/VEx data (Mahieux

et al., 2015), which report nightside temperature of  $118 \pm 15$  K above 130 km (Piccialli et al., 2015).

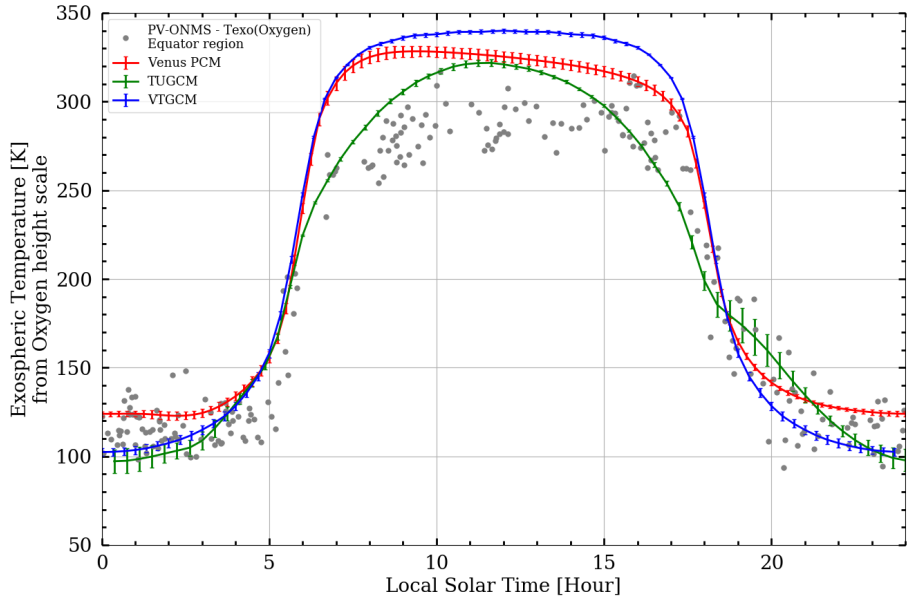


Figure 7: Diurnal variation of the Venusian exospheric temperature derived from the oxygen height scale (grey points) and predicted GCMs around equator for  $E10.7 = 200 \pm 15$  s.f.u): VPCM (blue line), VTGCM (red line) and TUGCM (green line). The gap between 6 and 7.5 LT is due to the lack of data. The "exospheric temperature" is the temperature averaged for layers above  $2 \times 10^{-6}$  Pa for each GCM. The predicted temperature spatial variability around  $30^\circ\text{S}$ - $30^\circ\text{N}$  is plotted with vertical bars. Figure adapted from Martinez et al. (2023).

This overestimation of dayside temperature is mainly due to underestimated cooling, notably from  $15 \mu\text{m}$   $\text{CO}_2$  emission, caused by low O number density for layers above  $1 \times 10^{-3}$  Pa (see Martinez et al., 2023). Nightside temperatures align with observations thanks to the fine-tuning of GW parameterization/Rayleigh friction (see details in Section 3.1) which reduce the zonal wind, and thus limit adiabatic compressional heating (e.g. dominant heating source during nighttime; Schubert et al., 1980). Without those parameterization, models tend to overpredict nightside thermospheric temperatures (Martinez et al., 2023).

#### 4.1.2. Solar Cycle effect on exospheric temperatures

Simulations/Retrieved	EUV index range [s.f.u]	Exospheric temperature sensitivity with solar activity [K/(s.f.u)]
VPCM nominal case	70-200	Dayside: 0.471 Nightside: $\leq 0.02$
VPCM nominal case	200-250	Dayside: 0.549 Nightside: $\leq 0.02$
VTGCM nominal case	70-200	Dayside: 0.694 Nightside: $\leq 0.02$
VTGCM nominal case	200-250	Dayside: 0.676 Nightside: $\leq 0.02$
TUGCM nominal case	70-200	Dayside: 0.804 Nightside: 0.048
VPCM with quenching rate $= 3 \times 10^{-12} \text{ cm}^3 \text{ s}^{-1}$	70-200	Dayside: 0.603 Nightside: $\leq 0.02$
VPCM with quenching rate $= 3 \times 10^{-12} \text{ cm}^3 \text{ s}^{-1}$	200-250	Dayside: 0.686 Nightside: $\leq 0.02$
Martinez et al. (2023) from PV-ONMS	Dayside: 180-260 Nightside: 150-280	Dayside: 0.43-0.58 Nightside: $\leq 0.02$
Mahajan et al. (1990) from PV-ONMS	Dayside: 180-260	Dayside: 0.5-0.6
Keating and Hsu (1993) (model)	130-180	Dayside: 0.6-0.7 Nightside: 0.15-0.2
Keating et al. (1985) and Hedin et al. (1983) (models)	Dayside: 180-260	Dayside: 0.4-0.58 Nightside: no variation

Table 4: Exospheric temperature sensitivity with solar activity ( $dT/dE_{10.7}$ ) for different tests and for the GCMs' nominal case described in Table 2. The values correspond to the simulated temperature averaged from  $2 \times 10^{-6}$  Pa up to the top level of each model, around the equator ( $30^\circ\text{S}$ - $30^\circ\text{N}$ ) and between 9-15 LT (21-3 LT) for dayside (nightside). See text for details.

Exospheric temperature sensitivity to solar activity ( $\frac{dT}{dE_{10.7}}$ ) can be derived from retrieved and simulated temperature as summarized in table 4. Previous studies using PV-ONMS reported sensitivities of 0.40-0.58 K/s.f.u (Keating et al., 1985; Hedin et al., 1983) while Martinez et al. (2023) and Mahajan et al. (1990) obtained a sensitivity of 0.43-0.58 K/s.f.u and 0.5-0.6 K/s.f.u respectively, depending on local time selection. None of these studies observed a significant nightside response, with changes below 0.05 K/s.f.u, well within uncertainty. For the GCMs discussed here, dayside sensitivities (for  $E_{10.7}$  between 70 and 200 s.f.u) are around 0.471 K/s.f.u for VPCM,

0.694 K/s.f.u for VTGCM and 0.804 K/s.f.u for TUGCM (see Figure 8). All nightside sensitivities are below 0.05 K/s.f.u.

Keating and Hsu (1993) updated the VIRA model to include long-term EUV variability, finding a sensitivity of 30-35 K over a 50 s.f.u (130-180 s.f.u), equivalent to  $\sim 0.6\text{-}0.7$  K/s.f.u at noon, and lower than 0.15-0.2 K/s.f.u at midnight. However, this stronger response, particularly on the nightside, is not supported by later observations (Piccialli et al., 2015).

Differences in temperature sensitivity to solar activity across GCMs are primarily driven by variations in their thermal budgets, governed by the balance between EUV heating, radiative cooling, and thermal conduction. From low to high solar activity, the peak EUV heating rate increases by a factor of 3 in TUGCM, 2.2 in VTGCM, and 1.7 in VPCM, explaining the higher temperature sensitivity in TUGCM and VTGCM. This underscores the importance of the chosen EUV solar spectrum in modeling temperature responses to the solar cycle. Radiative cooling, particularly via  $15\text{ }\mu\text{m}$   $\text{CO}_2$  emission, acts as a buffer against solar forcing, damping temperature variability with solar activity (Keating and Bougher, 1992; Bougher et al., 1986). For instance, by reducing the  $\text{CO}_2\text{-O}$  quenching coefficient in VPCM from  $5 \times 10^{-12}\text{ cm}^3\text{s}^{-1}$  to  $3 \times 10^{-12}\text{ cm}^3\text{s}^{-1}$  (as in the VTGCM and TUGCM), it increases the dayside temperature sensitivity to solar activity from 0.471 to 0.603 K/s.f.u. (see Table 4). Keating and Bougher (1992) showed that exospheric temperature response to short-term EUV variability can be reproduced with heating efficiency of 16-23% and an O- $\text{CO}_2$  quenching rates of  $1 - 4 \times 10^{-12}\text{ cm}^3\text{s}^{-1}$ . Fox (1988) similarly suggested 20-25% EUV heating efficiency and quenching rates ( $\geq 1 \times 10^{-12}\text{ cm}^3\text{s}^{-1}$ ).

As summarized in Table 2, VPCM uses a higher quenching rate (i.e.  $5 \times 10^{-12}\text{ cm}^3\text{s}^{-1}$  than VTGCM and TUGCM ( $3 \times 10^{-12}\text{ cm}^3\text{s}^{-1}$ ), leading to a smaller temperature variation with solar activity. Conversely, the lower atomic oxygen density of TUGCM reduces radiative cooling, amplifying its sensitivity.

#### 4.1.3. *Nightside and Dayside Vertical profile around the equator*

Figure 9 is adapted from Fig. 15 in Limaye et al. (2017) and shows a selection of observed (nighttime) and retrieved (dayside) temperature profiles together with nominal VPCM, VTGCM and TUGCM simulations on daytime and nighttime around the equator.

On the dayside, VPCM and VTGCM successfully reproduce the warm and cold layers observed near 110 km and 125-130 km. VPCM overestimates

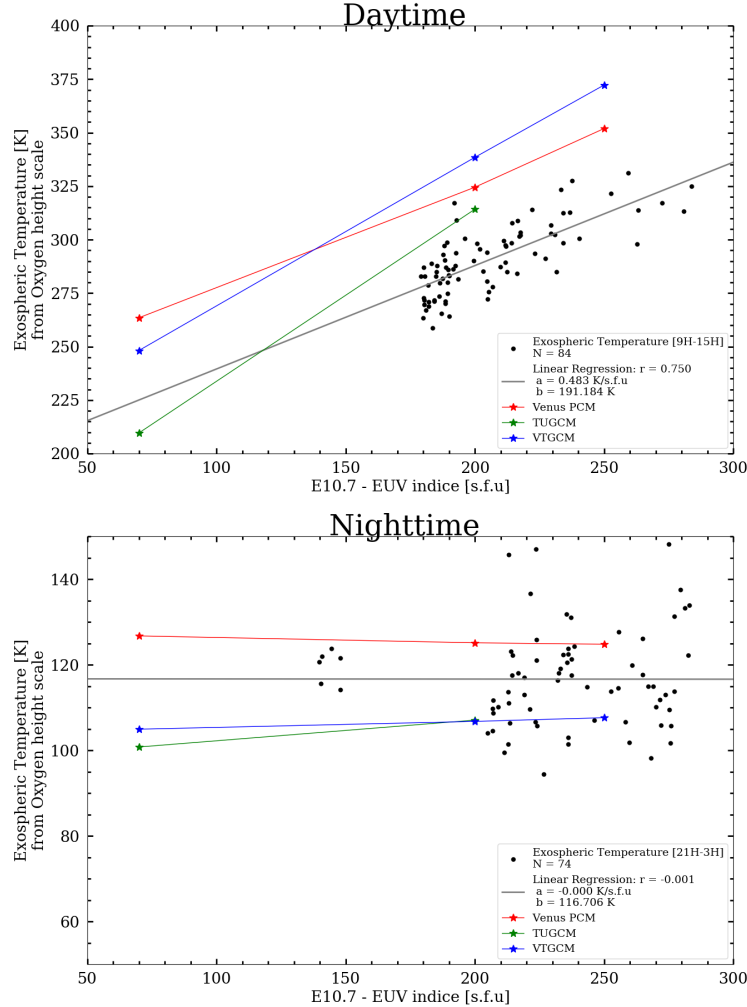


Figure 8: Dependence of exospheric temperature with E10.7 solar flux index. The black points correspond to the retrieved exospheric temperatures from PV-ONMS oxygen number density observations at 09-15 LT (top panel) and 21-03 LT (bottom panel). The gray line corresponds to the linear regression of the retrieved exospheric temperatures with the E10.7 solar flux index. The colored lines and markers correspond to the exospheric temperature predicted by each model for several E10.7 values (VPCM in red, VTGCM in blue and TUGCM in green). In its current state, TUGCM is unable to model beyond 200 s.f.u. The E10.7 solar flux index is adjusted for the Earth-Sun-Venus angle but remains standardized to 1 astronomic unit (after Martinez et al., 2023).

the warm peak altitude by 5 km, likely due to vertical resolution limits (3 km is  $\sim$ one scale height), but both models stay within observational uncertainties. Above  $\sim$ 100 km VTGCM and VPCM are warmer than VIRTIS-H and HHSMT data, though still within the large error bars of VIRTIS-H and HIPWAC-THIS.

TUGCM shows a different structure, with a temperature peak around 125 km, 15 km higher than HIPWAC-THIS observations. Below 120 km, it underestimates the temperatures by up to 30 K, while above 120 km it overestimates them. These differences can be explained by the significant pressure offset of the NIR heating rate compared with VTGCM/VPCM, which heats up at high altitude. Between approximately 120 and 140 km (corresponding to pressure  $5 \times 10^{-2}$  Pa and  $10^{-4}$  Pa at noon, as shown in Figure 6 in section 3.7), the contribution of conduction is at least one order of magnitude smaller than the radiative one. Therefore, the temperature difference in this region is related to radiative cooling of TUGCM being less significant than VTGCM and VPCM (see section 3.5).

As discussed in Section 4.1, nominal simulations reproduce the nightside cryosphere for layers above  $10^{-1}$  Pa. Below this level, VPCM aligns with SPICAV and VeRa observations, while the TUGCM underestimates nightside temperature by 15-25 K and fails to capture the local temperature bump. Above 110 km, VTGCM is cooler than SPICAV but remains within the observational uncertainty. Between 90 and 110 km, VTGCM agrees well with Heinrich Hertz Sub-Millimeter Radio Telescope (HHSMT), while below 90 km it underestimates temperature by 20-50 K compared to VEx/VeRa observations, possibly due to missing aerosol radiative effects, as suggested by Brecht et al. (2021). The weaker adiabatic heating of TUGCM around 10-0.1 Pa (see Figure S.5 in the supplementary material) may explain the lack of temperature bump around 1 Pa. Previous nightglow observations (e.g., Bailey et al., 2008; Bertaux et al., 2007) suggested that the temperature increase in the nightside was due to the adiabatic heating caused by the downward flow of the SS-AS wind. In other observations, HHSMT and James Clark Maxwell Telescope (JCMT) have also observed a warm layer around 100 km but the average magnitude is not consistent across the different observations (Bailey et al., 2008; Clancy et al., 2008; Rengel et al., 2008). Simulations with VTGCM in Brecht et al. (2011) also showed a nightside warm layer, interpreted as adiabatic heating from the enhanced day-to-night winds driven by the 4.3  $\mu$ m heating on the dayside.

In the 100-150 km altitude range, both on dayside and nightside, dis-

crepancies between VTS3/VIRA and the three models mainly stem from the empirical nature of VIRA and VTS3 at those upper layers. They are mainly based on PV measurements above 140 km and on model extrapolations assuming hydrostatic equilibrium between 100 and 140 km, due to a lack of observational data in this atmospheric region.

#### 4.2. *Composition*

Figure 10 and Figure 11 show the vertical profile of Venus' upper thermosphere composition ( $\text{CO}_2$ ,  $\text{N}_2$ ,  $\text{O}$  and  $\text{CO}$ ) observed by PV-ONMS (at high solar activity) and predicted by each nominal GCMs on the nightside and the dayside, respectively. A quick comparison between predictions and observations shows significant discrepancies. On the nightside, VTGCM and TUGCM generally underestimate  $\text{CO}$ ,  $\text{N}_2$  and  $\text{CO}_2$ , while VPCM aligns more closely with the upper limit of observed variability. However, VPCM underestimates atomic oxygen at 140 km, though it falls within the observed range at higher altitudes. These differences are partly explained by the cooler temperature in VTGCM and TUGCM for layers above  $10^{-2}$  Pa (above 115-120 km) compared with VPCM, causing a bias in altitude for the same pressure (see Section 3.7).

On the dayside, all models underestimate the amount of atomic oxygen in the Venusian thermosphere: by a factor of 2 approximately above 160 km for VTGCM/TUGCM, and a factor of 4 for VPCM. The  $\text{CO}_2$  and  $\text{N}_2$  densities predicted by VPCM are similar to observations between 150 and 160 km but they are different above 160 km. This discrepancy can be explained by an overestimated exospheric temperature, leading to a slower decrease in number density with altitude. The significant underestimation of  $\text{CO}$  by TUGCM is due to the underestimation of the photodissociation of  $\text{CO}_2$  into  $\text{O}$  and  $\text{CO}$  as explained in Section 3.2. The small mismatch in the atomic oxygen of TUGCM above 140 km is not physically realistic, given its predicted low oxygen production.

As noted in Section 3.2, atomic oxygen densities in VPCM and VTGCM differ by less than 50% at  $10^{-5}$  Pa and are relatively similar at  $10^{-6}$  Pa. The better agreement of VTGCM with PV-ONMS data for atomic oxygen and  $\text{CO}$  likely result from atmospheric expansion at higher temperature, which shifts pressure levels to higher altitude (see Section 3.7).

Under these conditions, VTGCM, TUGCM and VPCM likely underestimate atomic oxygen density for layers below  $10^{-5}$  Pa by a factor of at least 2-4.

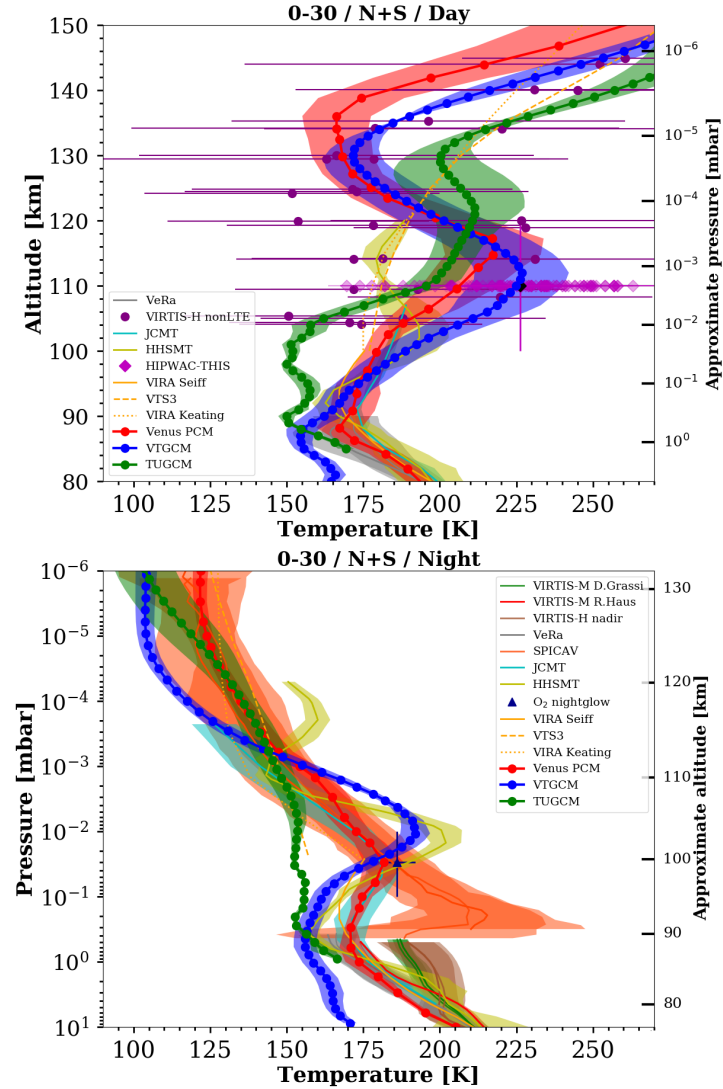


Figure 9: Compilation of available Venus temperature profiles above 80 km both from spacecrafts, ground based telescopes and retrieved from CO non-LTE emissions observed by VIRTIS/VEx versus dayside (7-17 LT; top) and nightside (21-3 LT; bottom) model predictions averaged at equatorial latitude from Southern and Northern hemisphere. Corresponding approximate values for altitude/pressure value is given on the right hand side of the panel. Panels are adapted from Fig. 15 in Limaye et al. (2017). Uncertainties (one standard deviation) are either plotted as colored areas for averaged profiles in the same bin (Venus Express datasets, JCMT, HHSMT). The models predicted profiles are in thick solid line with circle marker (VPCM in red, VTGCM in blue and TUGCM in green), their spatial variability over the selected zone are plotted as colored areas.

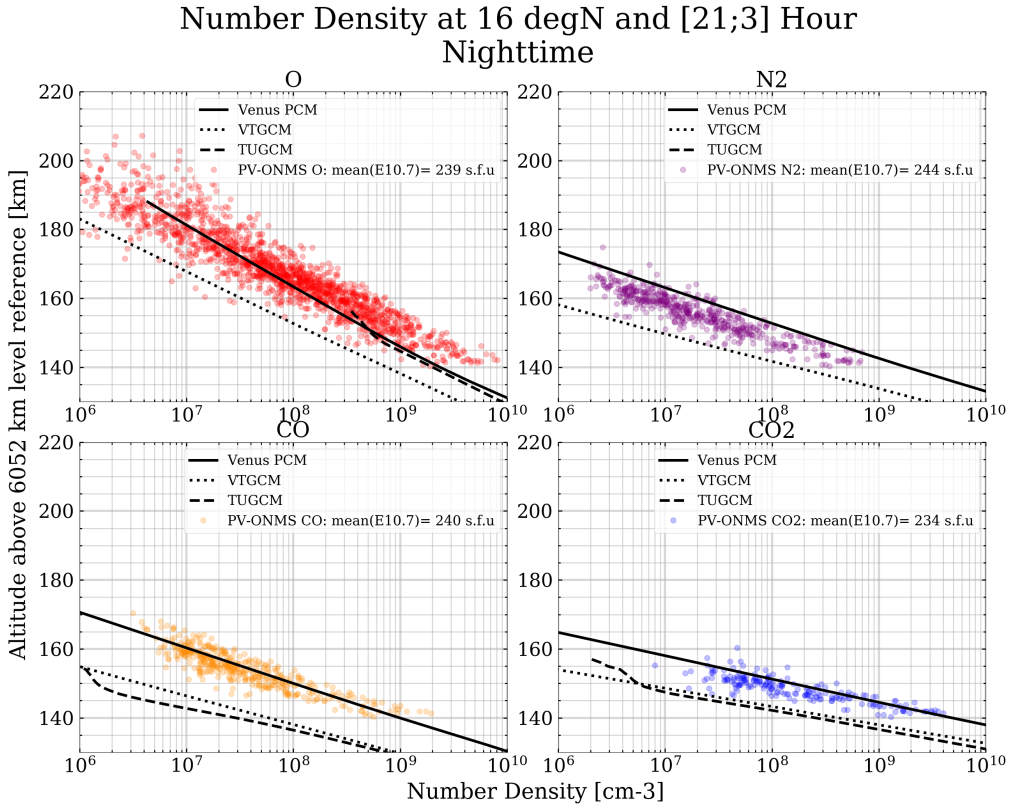


Figure 10: Vertical profiles of the upper thermosphere number density composition (top left corner: O; top right corner: N<sub>2</sub>; bottom left corner: CO; Bottom right corner: CO<sub>2</sub>) for nightside at high solar activity. The colored points correspond to the PV-ONMS observations. The lines correspond to the number densities predicted by nominal simulation (VPCM: full; VTGCM: dotted; TUGCM: dashed) at high solar activity. The N<sub>2</sub> dashed line is not present because TUGCM does not include N<sub>2</sub>. On the nightside, TUGCM's twisted shape above 150 km is linked to the fact that the model top varies between 150 km and 160 km, causing a bias average.

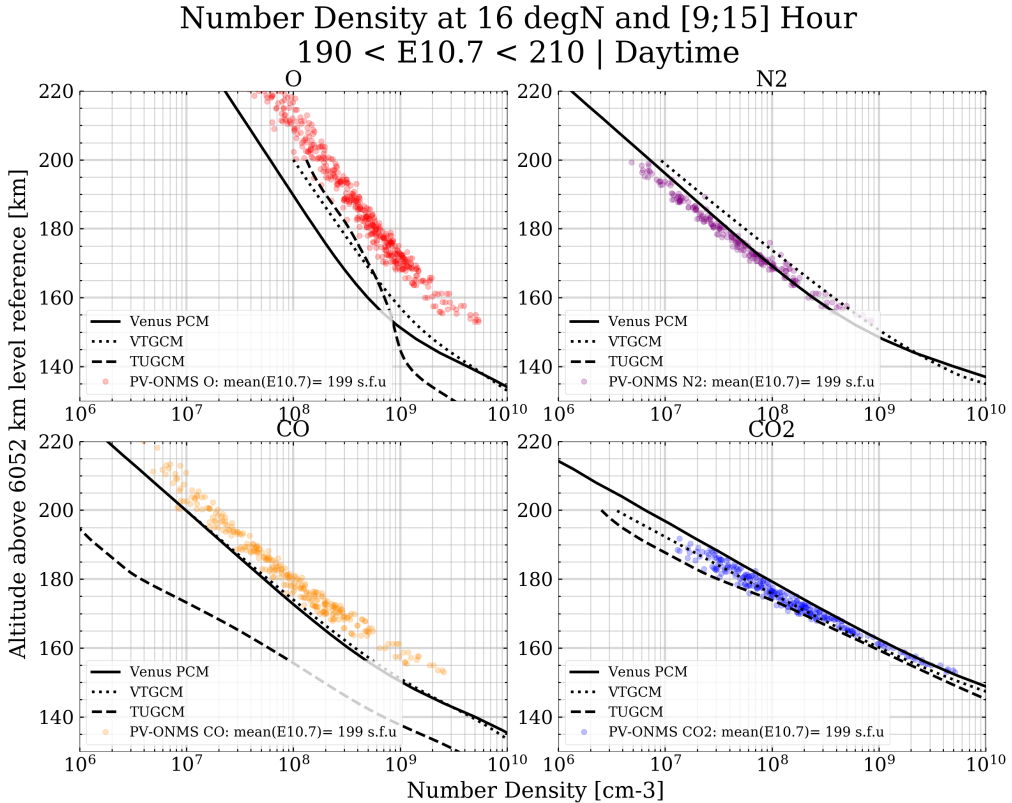


Figure 11: Vertical profiles of the upper thermosphere number density composition (top left corner: O; top right corner: N<sub>2</sub>; bottom left corner: CO; Bottom right corner: CO<sub>2</sub>) for dayside at high solar activity. The colored points correspond to the PV-ONMS observations. The lines correspond to the number densities predicted by nominal simulation (VPCM: full; VTGCM: dotted; TUGCM: dashed) at high solar activity. The N<sub>2</sub> dashed line is not present because TUGCM does not include N<sub>2</sub>. On the nightside, TUGCM's twisted shape above 150 km is linked to the fact that the model top varies between 150 km and 160 km, causing a bias average.

### 4.3. Mass Density

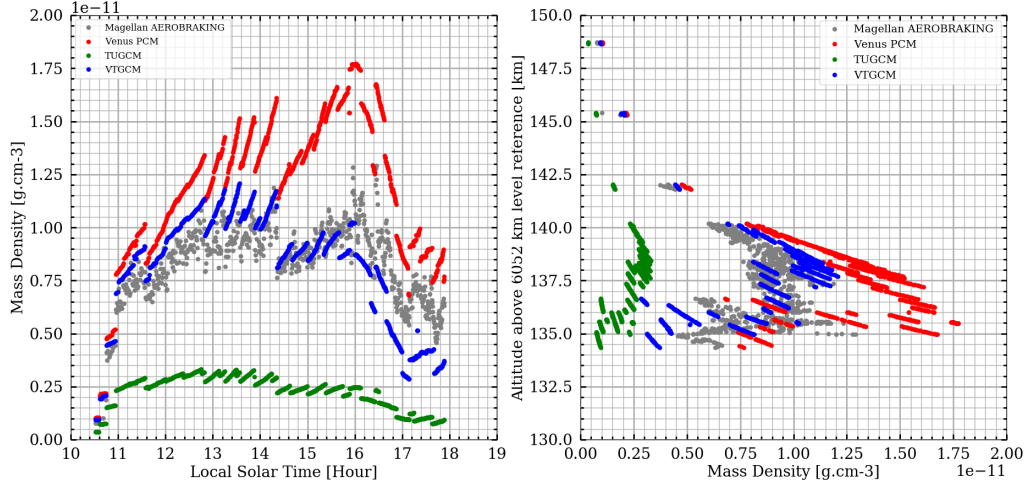


Figure 12: Comparison of local time variation (left) and vertical profile (right) of the mass density measured during the Magellan aerobraking campaign (gray point; Giorgini et al., 1995) with predicted values by each nominal model at low solar activity, plotted with colored points (VTGCM in blue, VPCM in red and TUGCM in green).

Figure 12 shows the mass density reconstructed from Magellan data, compared to model predictions. Mass density predicted by TUGCM is between 3 and 4 times lower than Magellan measurements between 135 and 145 km, while VPCM overestimate the mass density by 30 to 70% in the same region. VTGCM shows an excellent agreement with Magellan data between 11 LT and 16 LT, although its underestimates this mass density by up to 50% later than 16.5 LT.

A significant divergence between model predictions is observed, primarily due to the differences in temperature profiles below 135-145 km. These differences in mass density reflect whether the average temperature below a given altitude is over/under-estimated. The apparent agreement between 10 LT and 16 LT for VTGCM likely stems from its predicted mean temperature below 135 km being closer to actual Venusian conditions. However, since VTGCM underestimates the temperature below 100 km compared with observations (see Fig. 9), it is likely that it overestimates the mean temperature above 100 km for Magellan conditions. The underestimation of mass density beyond 16.5 LT for VTGCM may result from to zonal temperature variations near the equator. The mass density discrepancies are consequences of

different daytime predicted temperatures between 85 and 130 km, compared to Venusian conditions during Magellan campaign, being TUGCM and VTGCM colder and VPCM warmer, respectively.

Figure 13 shows the vertical profile of density mass as a function of altitude predicted by the three reference models on the nightside (top) and dayside (bottom) for different solar activity. Mass density reconstructions by Magellan (medium solar activity) and PV (high solar activity) are also included.

On the nightside, observations show no significant changes in mass density with solar activity. VPCM predicts densities within the observed variability range, though slightly lower than the average around 165 km. Similar to the results for atmospheric composition, both VTGCM and TUGCM underestimate nightside mass density. This can be attributed to their lower predicted nightside temperatures compared to VPCM, leading to a more contracted atmosphere (see Fig. 6 and Fig. 9). Notably, VPCM includes a significant amount of Helium on the nightside, whose density, according to observations, exceeds that of atomic oxygen above 180 km and CO/N<sub>2</sub> above 160 km. The absence of helium in VTGCM and TUGCM likely contributes to their underestimation of mass density at higher altitudes.

On the dayside, all three models underestimate the variation in mass density with solar activity, with VPCM showing the smallest variation in mass density in comparison to TUGCM and VTGCM. Since mass density variations stem from changes in both atmospheric composition and temperature, the exospheric temperature sensitivity to solar activity predicted by each model (see section 4.1.2 and table 4) will mainly determine the change in mass density. With the weaker exospheric temperature sensitivity to solar activity, VPCM has the smaller change in mass density while the larger mass density variability in VTGCM and TUGCM is likely due to their larger predicted temperature variations. VTGCM shows good agreement with the PV-OAD data under high solar activity and exhibits the most realistic response to the solar cycle. As with atmospheric composition, some of the differences among the models are accentuated by vertical shifts in altitude grid, but the primary cause of the mass density underestimation in VPCM, VTGCM, and TUGCM is the insufficient representation of atomic oxygen (as seen in Fig. 11).

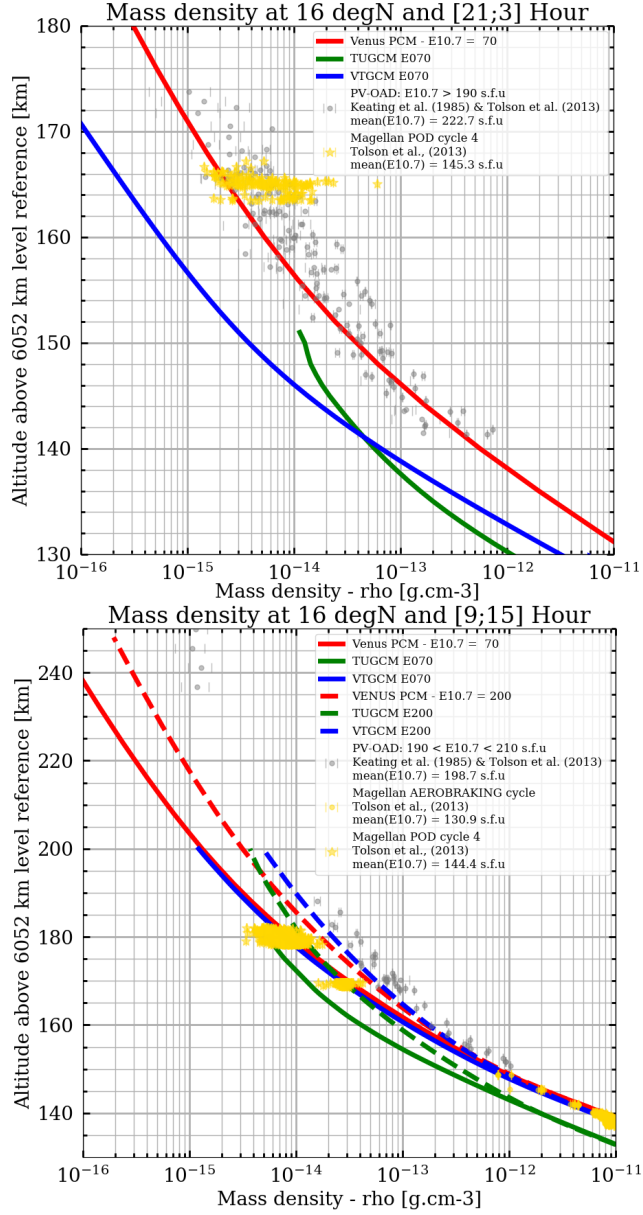


Figure 13: Vertical profiles of the mass density for nightside (21-03h LT; top) and dayside (9-15h LT; bottom). The gray points correspond to the PV-OAD measurements at high solar activity. The yellow points correspond to the Magellan measurements (120-160 s.f.u). The lines correspond to the mass density predicted by nominal simulation (VPCM: red; VTGCM: blue; TUGCM: green) for high (dashed lines) and low (solid lines) solar activity.

## 5. Conclusions and Recommendations

We have presented and analyzed nominal simulations of the Venusian mesosphere/thermosphere from different models, comparing composition, thermal structures, solar activity effects, and the contribution of the key heating and cooling processes. Similarities and discrepancies between models were discussed. In their current form, the nominal models struggle to reproduce both the composition and temperature observations of Pioneer Venus (above 140 km), and capture solar cycle variations.

On the dayside, thermospheric temperatures are generally overestimated, primarily due to an underestimation of atomic oxygen density, which controls the CO<sub>2</sub> NLTE cooling. VPCM shows the lowest sensitivity to solar activity, while VTGCM and TUGCM tend to overestimate it, mainly due to differences in the EUV spectra used for heating rates. Among the models, VTGCM provides the best match to PV mass density under high solar activity, though it still slightly underestimate it.

On the nightside, all three models predict exospheric temperatures within the uncertainty range of Pioneer Venus and Venus Express data. Between 100 km and 140 km altitude, VPCM and VTGCM show good agreement with nightside and dayside temperature profiles and a slightly overestimate the mass density between 135 and 145 km compared to Magellan data. TUGCM however shows a significant pressure-altitude offset and underestimates temperature, mostly due to its NIR heating parameterization. Below 100 km, VPCM matches observed temperatures well, while VTGCM and TUGCM tend to underestimate the temperature by a few tens of Kelvin. Nevertheless, VTGCM captures the observed temperature variability, as noted by Brecht et al. (2021).

This study highlights the challenges in accurately modeling Venus' upper atmosphere. Comparing GCM outputs with observations reveals how modeling choices (such as the EUV spectral input, NLTE CO<sub>2</sub> radiative cooling, and treatment of atomic oxygen) impact simulated thermal structures. Atomic oxygen remains a key variable, central to heating, cooling, and chemistry. While sensitivity tests with non-orographic gravity wave parameters are not included here, these unconstrained inputs significantly affect zonal winds and nightside temperatures.

Ongoing model development and intercomparison efforts are essential to improving our understanding of Venus's poorly observed upper layers. Models encapsulate our current knowledge and help identify gaps, while observa-

tions provide critical constraints that guide future improvements. Data assimilation techniques, which incorporate observations into a numerical model, would help estimating undetermined parameters by the observations (Fujisawa et al., 2023). A previous study using Akatsuki data (Fujisawa et al., 2022) showed that this technique significantly improves the modeled structures of thermal tides and general circulation, even with limited data.

Based on the analysis in this study, we propose the following priorities for improving Venus upper atmosphere modeling:

- 1. Standardize the EUV-UV Solar Spectrum input**

The models show varying upper atmosphere temperature sensitivities to the solar cycle, largely due to differences in the EUV-UV spectral input. We recommend using a consistent solar reference spectrum, covering at least one period of the solar cycle, such as those provided by the NASA NOAA LASP (NNL; <https://lasp.colorado.edu/lisird/>), which incorporates data from missions like "Thermosphere Ionosphere Mesosphere Energetics and Dynamics" (TIMED) and "Solar Dynamics Observatory" (SDO). Applying the method like González-Galindo et al. (2013) to scale these inputs with solar activity would improve consistency, reduce uncertainties, and better constrain EUV-UV heating budget, photodissociation and photoionization processes.

- 2. Update the NIR Heating Scheme with VEx-Era Data**

The current NIR heating parameterizations used as reference for the Venusian upper atmosphere (e.g. Roldán et al., 2000), rely on outdated composition and temperature profiles. Updating this framework using Venus Express data (especially between 100–150 km) would improve model accuracy. Incorporating the dependence of 2.7 and 4.3  $\mu\text{m}$  heating on atomic oxygen could enhance variability predictions, though the lack of O measurements in the 90–150 km range and at low solar activity remains a limitation. In the interim, applying the current best estimates of atomic oxygen to constrain NIR heating is the most viable approach. A dedicated mission measuring both temperature and composition, especially atomic oxygen, remains a key priority.

- 3. Harmonize and Reassess Radiative Cooling Schemes**

$\text{CO}_2$  radiative cooling at 15  $\mu\text{m}$  is crucial for regulating thermospheric temperatures. Among the three models, VPCM uses the most advanced parameterization, while VTGCM and TUGCM rely on simpli-

fied schemes. A direct intercomparison of cooling rates using a shared composition and temperature profiles would help quantify differences. Furthermore, revisiting and updating reaction rates governing the energy levels of CO<sub>2</sub>, N<sub>2</sub>, CO and O (based on recent findings from López-Puertas et al., 2024) could improve accuracy.

#### 4. Investigate the underestimated Atomic Oxygen

Atomic oxygen, essential for heating and cooling processes, is consistently underestimated across all models. Its abundance depends on chemical and ionospheric production, transport, and (to a lesser extent) destruction. While electron impact (e.g. alternative source of CO, O and N) is currently excluded, its contribution appears too minor to explain the discrepancies. We recommend focusing on the role of transport (through advection and molecular diffusion) in shaping the vertical and diurnal distribution of atomic oxygen, while remaining open to re-evaluating other potential sources.

#### Acknowledgments

G.G and A.M are funded by Junta de Andalucía through the program EMERGIA 2021 (EMC21 00249). The IAA team (A.M, G.G, A.S, F.G.G) also acknowledges financial support from the Severo Ochoa grant CEX2021-001131-S funded by MCIN/AEI/ 10.13039/501100011033, and the Spanish Prototype of an SRC (SPSRC) service and support funded by the Ministerio de Ciencia, Innovación y Universidades (MCIU), by the Junta de Andalucía, by the European Regional Development Funds (ERDF) and by the European Union NextGenerationEU/PRTR. A.S is financed by project AST-00001-X with funding from the EU NextGenerationEU, the MCIU - Gobierno de España, the Plan de Recuperación y Resiliencia, the AEI, CSIC and the Consejería de Universidad, Investigación e Innovación de la Junta de Andalucía. A.S acknowledges the support of project PID2021-126365NB-C21 funded by MCIN/AEI/10.13039/501100011033/ and FEDER. F.G.-G. acknowledges financial support from grant PID2022-137579NB-I00.

T.K. is funded by Japan Society for the Promotion of Science (JSPS) (KAKENHI grant No. JP23K25932). H.K. is funded by JSPS (KAKENHI grant No. JP23KJ0201) and International Joint Graduate Program in Earth and Environmental Sciences (GP-EES) of Tohoku University. The authors thank N. Hoshino who originally developed TUGCM, and Y. Kasaba, M. Takagi

and H. Sagawa for helpful discussions during the early phase of the project. The Venus PCM simulations were done thanks to the High-Performance Computing (HPC) resources of “Tres Grand Centre de Calcul” (TGCC) under the allocation No. A0140110391 made by Grand Equipement National de Calcul Intensif (GENCI). The “PVO-V-POS-5-VSOCOORDS-12SEC-V1.0” and “PVO-V-OIMS-4-ION DENSITY-12S-V1.0” are obtained from the Planetary Data System (PDS) (<https://pds.nasa.gov/>). This work was partly funded by ESA under the contract No. 4000138542/22/NL/CRS.

## Open Research Section

The Venus Planetary Climate Model (PCM) can be accessed freely via <svn.lmd.jussieu.fr/Planeto/trunk>. For this study, nominal simulations were performed using the code revision 3035. The results are fully reproducible by running the model with its distributed data files. The outputs from Venus PCM use in this paper are available in NetCDF format via Zenodo (Martinez et al., 2025).

The Venus Thermospheric Global Model outputs used in this paper can be accessed freely in NetCDF format via Deep Blue Data website at Brecht and Bouger (2025).

The outputs from Tohoku University Global Circulation Model used in this paper are available in text format via Zenodo (Karyu, 2025).

## References

Alexander, M.J., Stewart, A.I.F., Bouger, S.W., 1992. Local-time asymmetries in the Venus thermosphere. *LPI Contributions* 789, 1–2.

Bailey, J., Meadows, V.S., Chamberlain, S., Crisp, D., 2008. The temperature of the Venus mesosphere from O<sub>2</sub> (aΔg1) airglow observations. *Icarus* 197, 247–259. doi:10.1016/j.icarus.2008.04.007.

Banks, P., Kockarts, G., 1973. Aeronomy. Academic Press. URL: <https://books.google.es/books?id=5BXgBAAAQBAJ>.

Bertaux, J.L., Nevejans, D., Koralev, O., Villard, E., Quémérais, E., Neefs, E., Montmessin, F., Leblanc, F., Dubois, J.P., Dimarellis, E., Hauchecorne, A., Lefèvre, F., Rannou, P., Chaufray, J.Y., Cabane, M., Cernogora, G., Souchon, G., Semelin, F., Reberac, A., van Ransbeek, E., Berkenbosch, S.,

Clairquin, R., Muller, C., Forget, F., Hourdin, F., Talagrand, O., Rodin, A., Fedorova, A., Stepanov, A., Vinogradov, I., Kiselev, A., Kalinnikov, Y., Durry, G., Sandel, B., Stern, A., Gérard, J.C., 2007. SPICAV on Venus Express: Three spectrometers to study the global structure and composition of the Venus atmosphere. *Planetary and Space Science* 55, 1673–1700. doi:10.1016/j.pss.2007.01.016.

Bougher, S.W., Borucki, W.J., 1994. Venus o2 visible and ir night-glow: Implications for lower thermosphere dynamics and chemistry. *Journal of Geophysical Research: Planets* 99, 3759–3776. doi:<https://doi.org/10.1029/93JE03431>.

Bougher, S.W., Brecht, A.S., Schulte, R., Fischer, J., Parkinson, C.D., Mahieux, A., Wilquet, V., Vandaele, A., 2015. Upper atmosphere temperature structure at the Venusian terminators: A comparison of SOIR and VTGCM results. *Planetary and Space Science* 113, 336–346. doi:10.1016/j.pss.2015.01.012.

Bougher, S.W., Dickinson, R.E., Ridley, E.C., Roble, R.G., 1988. Venus mesosphere and thermosphere III. Three-dimensional general circulation with coupled dynamics and composition. *Icarus* 73, 545–573. doi:10.1016/0019-1035(88)90064-4.

Bougher, S.W., Dickinson, R.E., Ridley, E.C., Roble, R.G., Nagy, A.F., Cravens, T.E., 1986. Venus mesosphere and thermosphere. II - Global circulation, temperature, and density variations. *Icarus* 68, 284–312. doi:10.1016/0019-1035(86)90025-4.

Bougher, S.W., Engel, S., Roble, R.G., Foster, B., 1999. Comparative terrestrial planet thermospheres 2. Solar cycle variation of global structure and winds at equinox. *Journal of Geophysical Research* 104, 16591–16611. doi:10.1029/1998JE001019.

Brecht, A.S., 2011. Tracing the dynamics in Venus' upper atmosphere. Ph.D. thesis. University of Michigan.

Brecht, A.S., Bougher, S.W., 2012. Dayside thermal structure of Venus' upper atmosphere characterized by a global model. *Journal of Geophysical Research (Planets)* 117, 8002. doi:10.1029/2012JE004079.

Brecht, A.S., Bougher, S.W., 2025. Comparison of general circulation models of the venus upper atmosphere: A collection of VTGCM datasets[data set]. University of Michigan - Deep Blue Data doi:10.7302/3jd7-fn88.

Brecht, A.S., Bougher, S.W., Gérard, J.C., Parkinson, C.D., Rafkin, S., Foster, B., 2011. Understanding the variability of nightside temperatures, NO UV and O<sub>2</sub> IR nightglow emissions in the Venus upper atmosphere. *Journal of Geophysical Research (Planets)* 116, 8004. doi:10.1029/2010JE003770.

Brecht, A.S., Bougher, S.W., Shields, D., Liu, H.L., Lee, C., 2021. Planetary-scale wave impacts on the venusian upper mesosphere and lower thermosphere. *Journal of Geophysical Research: Planets* 126, e2020JE006587. doi:<https://doi.org/10.1029/2020JE006587>.

Chapman, S., Cowling, T.G., 1970. The mathematical theory of non-uniform gases. an account of the kinetic theory of viscosity, thermal conduction and diffusion in gases.

Clancy, R.T., Sandor, B.J., Moriarty-Schieven, G.H., 2008. Venus upper atmospheric CO, temperature, and winds across the afternoon/evening terminator from June 2007 JCMT sub-millimeter line observations. *Planetary and Space Science* 56, 1344–1354. doi:10.1016/j.pss.2008.05.007.

Clark, I.D., Noxon, J.F., 1970. Photodissociation of CO<sub>2</sub> on Mars. *Journal of Geophysical Research* 75, 7307. doi:10.1029/JA075i034p07307.

Dickinson, R.E., Bougher, S.W., 1986. Venus mesosphere and thermosphere 1. Heat budget and thermal structure. *Journal of Geophysical Research* 91, 70–80. doi:10.1029/JA091iA01p00070.

Dickinson, R.E., Ridley, E.C., 1972. Numerical Solution for the Composition of a Thermosphere in the Presence of a Steady Subsolar to-Antisolar Circulation with Application to Venus. *Journal of the Atmospheric Sciences* 29, 1557–1570. doi:10.1175/1520-0469(1972)029j1557:NSFTCO;2.0.CO;2.

Dickinson, R.E., Ridley, E.C., Roble, R.G., 1981. A three-dimensional general circulation model of the thermosphere. *Journal of Geophysical Research* 86, 1499–1512. doi:10.1029/JA086iA03p01499.

Felder, W., Morrow, W., Young, R.A., 1970. Experimental evidence of the photochemical instability of a pure CO<sub>2</sub> planetary atmosphere. *Journal of Geophysical Research* 75, 7311. doi:10.1029/JA075i034p07311.

Forget, F., Hourdin, F., Fournier, R., Hourdin, C., Talagrand, O., Collins, M., Lewis, S.R., Read, P.L., Huot., J.P., 1999. Improved general circulation models of the Martian atmosphere from the surface to above 80 km. *J. Geophys. Res.* 104, 24,155–24,176.

Fox, J.L., 1988. Heating efficiencies in the thermosphere of Venus reconsidered. *Planet Space Sci* 36, 37–46. doi:10.1016/0032-0633(88)90144-4.

Fox, J.L., 2007. Near-terminator Venus ionosphere: How Chapman-esque? *Journal of Geophysical Research (Planets)* 112, E04S02. doi:10.1029/2006JE002736.

Fox, J.L., Sung, K.Y., 2001. Solar activity variations of the Venus thermosphere/ionosphere. *Journal of Geophysical Research (Space Physics)* 106, 21305–21336. doi:10.1029/2001JA000069.

Fujisawa, Y., Murakami, S.y., Sugimoto, N., Takagi, M., Imamura, T., Horinouchi, T., Hashimoto, G.L., Ishiwatari, M., Enomoto, T., Miyoshi, T., Kashimura, H., Hayashi, Y.Y., 2022. The first assimilation of akatsuki single-layer winds and its validation with venusian atmospheric waves excited by solar heating. *Scientific Reports* 12. URL: <http://dx.doi.org/10.1038/s41598-022-18634-6>, doi:10.1038/s41598-022-18634-6.

Fujisawa, Y., Sugimoto, N., Ao, C.O., Hosono, A., Ando, H., Takagi, M., Garate-Lopez, I., Lebonnois, S., 2023. Evaluation of new radio occultation observations among small satellites at venus by data assimilation. *Icarus* 406, 115728. doi:<https://doi.org/10.1016/j.icarus.2023.115728>.

Garcia, R.F., Drossart, P., Piccioni, G., López-Valverde, M., Occhipinti, G., 2009. Gravity waves in the upper atmosphere of Venus revealed by CO<sub>2</sub> nonlocal thermodynamic equilibrium emissions. *Journal of Geophysical Research (Planets)* 114, E00B32. doi:10.1029/2008JE003073.

García-Comas, M., López-Puertas, M., Marshall, B.T., Wintersteiner, P.P., Funke, B., Bermejo-Pantaleón, D., Mertens, C.J., Remsberg, E.E., Gordley, L.L., Mlynczak, M.G., Russell, J.M., 2008. Errors in Sounding of

the Atmosphere using Broadband Emission Radiometry (SABER) kinetic temperature caused by non-local-thermodynamic-equilibrium model parameters. *Journal of Geophysical Research (Atmospheres)* 113, D24106. doi:10.1029/2008JD010105.

Gilli, G., Lebonnois, S., González-Galindo, F., López-Valverde, M.A., Stolzenbach, A., Lefèvre, F., Chaufray, J.Y., Lott, F., 2017. Thermal structure of the upper atmosphere of Venus simulated by a ground-to-thermosphere GCM. *Icarus* 281, 55–72. doi:10.1016/j.icarus.2016.09.016.

Gilli, G., López-Valverde, M.A., Peralta, J., Bouger, S., Brecht, A., Drossart, P., Piccioni, G., 2015. Carbon monoxide and temperature in the upper atmosphere of Venus from VIRTIS/Venus Express non-LTE limb measurements. *Icarus* 248, 478–498. doi:10.1016/j.icarus.2014.10.047.

Gilli, G., Navarro, T., Lebonnois, S., Quirino, D., Silva, V., Stolzenbach, A., Lefèvre, F., Schubert, G., 2021. Venus upper atmosphere revealed by a GCM: II. Model validation with temperature and density measurements. *Icarus* 366, 114432. doi:10.1016/j.icarus.2021.114432, [arXiv:2103.15649](https://arxiv.org/abs/2103.15649).

Giorgini, J., Wong, S.K., You, T.H., Chadbourne, P., Lim, L., 1995. Magellan aerobrake navigation. *Journal of the British Interplanetary Society* 48, 111–122.

González-Galindo, F., Chaufray, J.Y., López-Valverde, M.A., Gilli, G., Forget, F., Leblanc, F., Modolo, R., Hess, S., Yagi, M., 2013. Three-dimensional Martian ionosphere model: I. The photochemical ionosphere below 180 km. *Journal of Geophysical Research (Planets)* 118, 2105–2123. doi:10.1002/jgre.20150.

González-Galindo, F., López-Valverde, M.A., Angelats i Coll, M., Forget, F., 2005. Extension of a Martian general circulation model to thermospheric altitudes: UV heating and photochemical models. *Journal of Geophysical Research (Planets)* 110, E09008. doi:10.1029/2004JE002312.

Hedin, A.E., Niemann, H.B., Kasprzak, W.T., Seiff, A., 1983. Global empirical model of the Venus thermosphere. *Journal of Geophysical Research* 88, 73–83. doi:10.1029/JA088iA01p00073.

Hoshino, N., 2011. GCM simulations of the atmospheric coupling between the Venusian lower atmosphere and thermosphere through

atmospheric waves. Ph.D. thesis. Tohoku University. URL: <https://tohoku.repo.nii.ac.jp/records/7026>.

Hoshino, N., Fujiwara, H., Takagi, M., Kasaba, Y., 2013. Effects of gravity waves on the day-night difference of the general circulation in the Venusian lower thermosphere. *Journal of Geophysical Research (Planets)* 118, 2004–2015. doi:10.1002/jgre.20154.

Hoshino, N., Fujiwara, H., Takagi, M., Takahashi, Y., Kasaba, Y., 2012. Characteristics of planetary-scale waves simulated by a new venusian mesosphere and thermosphere general circulation model. *Icarus* 217, 818–830. doi:10.1016/j.icarus.2011.06.039.

Inn, E.C.Y., Heimerl, J.M., 1971. The photolysis of CO<sub>2</sub> at wavelengths exceeding 1740 Å. *Journal of the Atmospheric Sciences* 28, 838–841. doi:10.1175/1520-0469(1971)028j0838:TPOCAW;2.0.CO;2.

Karyu, H., 2025. Dataset for martinez et al. (2025) [data set]. URL: <https://doi.org/10.5281/zenodo.17153805>, doi:10.5281/zenodo.17153805.

Kasprzak, W.T., Hedin, A.E., Mayr, H.G., Niemann, H.B., 1988. Wavelike perturbations observed in the neutral thermosphere of Venus. *Journal of Geophysical Research* 93, 11237–11245. doi:10.1029/JA093iA10p11237.

Kasprzak, W.T., Keating, G.M., Hsu, N.C., Stewart, A.I.F., Colwell, W.B., Bouger, S.W., 1997. Solar Activity Behavior of the Thermosphere, in: Bouger, S.W., Hunten, D.M., Phillips, R.J. (Eds.), *Venus II: Geology, Geophysics, Atmosphere, and Solar Wind Environment*, p. 225.

Keating, G.M., Bertaux, J.L., Bouger, S.W., Dickinson, R.E., Cravens, T.E., Hedin, A.E., 1985. Models of Venus neutral upper atmosphere - Structure and composition. *Advances in Space Research* 5, 117–171. doi:10.1016/0273-1177(85)90200-5.

Keating, G.M., Bouger, S.W., 1992. Venus thermospheric response to short-term solar variations. *Advances in Space Research* 12, 111–128. doi:10.1016/0273-1177(92)90326-S.

Keating, G.M., Hsu, N.C., 1993. The Venus atmospheric response to solar cycle variations. *Geophysical Research Letters* 20, 2751–2754. doi:10.1029/93GL03010.

Lebonnois, S., Hourdin, F., Eymet, V., Crespin, A., Fournier, R., Forget, F., 2010. Superrotation of Venus' atmosphere analyzed with a full general circulation model. *Journal of Geophysical Research (Planets)* 115, 6006. doi:10.1029/2009JE003458.

Lebonnois, S., Sugimoto, N., Gilli, G., 2016. Wave analysis in the atmosphere of Venus below 100-km altitude, simulated by the LMD Venus GCM. *Icarus* 278, 38–51. doi:10.1016/j.icarus.2016.06.004.

Lee, C., Richardson, M.I., 2010. A general circulation model ensemble study of the atmospheric circulation of Venus. *Journal of Geophysical Research (Planets)* 115, E04002. doi:10.1029/2009JE003490.

Lee, C., Richardson, M.I., 2011. A Discrete Ordinate, Multiple Scattering, Radiative Transfer Model of the Venus Atmosphere from 0.1 to  $260\mu\text{m}$ . *Journal of the Atmospheric Sciences* 68, 1323–1339. doi:10.1175/2011JAS3703.1.

Limaye, S.S., Lebonnois, S., Mahieux, A., Pätzold, M., Bouger, S., Bruinsma, S., Chamberlain, S., Clancy, R.T., Gérard, J.C., Gilli, G., Grassi, D., Haus, R., Herrmann, M., Imamura, T., Kohler, E., Krause, P., Migliorini, A., Montmessin, F., Pere, C., Persson, M., Piccialli, A., Rengel, M., Rodin, A., Sandor, B., Sornig, M., Svedhem, H., Tellmann, S., Tanga, P., Vandaele, A.C., Widemann, T., Wilson, C.F., Müller-Wodarg, I., Zasova, L., 2017. The thermal structure of the venus atmosphere: Intercomparison of venus express and ground based observations of vertical temperature and density profiles. *Icarus* 294, 124 – 155. URL: <http://www.sciencedirect.com/science/article/pii/S0019103516307138>, doi:<http://dx.doi.org/10.1016/j.icarus.2017.04.020>.

López-Puertas, M., Fabiano, F., Fomichev, V., Funke, B., Marsh, D.R., 2024. An improved and extended parameterization of the  $\text{CO}_2$   $15\mu\text{m}$  cooling in the middle and upper atmosphere (co2\_cool\_fort-1.0). *Geoscientific Model Development* 17, 4401–4432. URL: <https://gmd.copernicus.org/articles/17/4401/2024/>, doi:10.5194/gmd-17-4401-2024.

Lott, F., Guez, L., 2013. A stochastic parameterization of the gravity waves due to convection and its impact on the equatorial stratosphere. *Journal of Geophysical Research (Atmospheres)* 118, 8897–8909. doi:10.1002/jgrd.50705.

Lott, F., Guez, L., Maury, P., 2012. A stochastic parameterization of non-orographic gravity waves: Formalism and impact on the equatorial stratosphere. *Geophysical Research Letters* 39, L06807. doi:10.1029/2012GL051001.

Mahajan, K.K., Kasprzak, W.T., Brace, L.H., Niemann, H.B., Hoegy, W.R., 1990. Response of Venus exospheric temperature measured by neutral mass spectrometer to solar EUV flux measured by Langmuir probe on the Pioneer Venus orbiter. *Journal of Geophysical Research* 95, 1091–1095. doi:10.1029/JA095iA02p01091.

Mahieux, A., Vandaele, A.C., Bouger, S.W., Drummond, R., Robert, S., Wilquet, V., Chamberlain, S., Picciali, A., Montmessin, F., Tellmann, S., Pätzold, M., Häusler, B., Bertaux, J.L., 2015. Update of the Venus density and temperature profiles at high altitude measured by SOIR on board Venus Express. *Planetary and Space Science* 113, 309–320. doi:10.1016/j.pss.2015.02.002.

Mahieux, A., Vandaele, A.C., Robert, S., Wilquet, V., Drummond, R., Montmessin, F., Bertaux, J.L., 2012. Densities and temperatures in the Venus mesosphere and lower thermosphere retrieved from SOIR on board Venus Express: Carbon dioxide measurements at the Venus terminator. *Journal of Geophysical Research (Planets)* 117, 7001. doi:10.1029/2012JE004058.

Martinez, A., Chaufray, J.Y., Lebonnois, S., González-Galindo, F., Lefèvre, F., Gilli, G., 2024. Three-dimensional Venusian ionosphere model. *Icarus* 415, 116035. doi:10.1016/j.icarus.2024.116035.

Martinez, A., Gilli, G., Lebonnois, S., 2025. Comparison of general circulation models of the venus upper atmosphere: A collection of VPCM datasets [data set]. URL: <https://doi.org/10.5281/zenodo.17142989>, doi:10.5281/zenodo.17142989.

Martinez, A., Lebonnois, S., Millour, E., Pierron, T., Moisan, E., Gilli, F., Lefèvre, F., 2023. Exploring the variability of the venusian thermosphere with the IPSL Venus GCM. *Icarus* 389, 115272. doi:10.1016/j.icarus.2022.115272.

Medvedev, A.S., Klaassen, G.P., 1995. Vertical evolution of gravity wave spectra and the parameterization of associated wave drag. *Journal of Geophysical Research (Atmospheres)* 100, 25,841–25,853. doi:10.1029/95JD02533.

Medvedev, A.S., Klaassen, G.P., 2000. Parameterization of gravity wave momentum deposition based on nonlinear wave interactions: basic formulation and sensitivity tests. *Journal of Atmospheric and Solar-Terrestrial Physics* 62, 1015–1033. doi:10.1016/S1364-6826(00)00067-5.

Mendonça, J.M., Read, P.L., 2016. Exploring the Venus global super-rotation using a comprehensive general circulation model. *Planetary and Space Science* 134, 1–18. doi:10.1016/j.pss.2016.09.001, arXiv:1609.06549.

Müller-Wodarg, I.C.F., Bruinsma, S., Marty, J.C., Svedhem, H., 2016. In situ observations of waves in Venus's polar lower thermosphere with Venus Express aerobraking. *Nature Physics* 12, 767–771. doi:10.1038/nphys3733.

Navarro, T., Gilli, G., Schubert, G., Lebonnois, S., Lefèvre, F., Quirino, D., 2021. Venus' upper atmosphere revealed by a GCM: I. Structure and variability of the circulation. *Icarus* 366, 114400. doi:10.1016/j.icarus.2021.114400.

Niemann, H.B., Kasprzak, W.T., Hedin, A.E., Hunten, D.M., Spencer, N.W., 1980. Mass spectrometric measurements of the neutral gas composition of the thermosphere and exosphere of Venus. *Journal of Geophysical Research* 85, 7817–7827. doi:10.1029/JA085iA13p07817.

Peralta, J., Hueso, R., Sánchez-Lavega, A., Piccioni, G., Lanciano, O., Drossart, P., 2008. Characterization of mesoscale gravity waves in the upper and lower clouds of Venus from VEX-VIRTIS images. *Journal of Geophysical Research (Planets)* 113, E00B18. doi:10.1029/2008JE003185.

Persson, M., 2015. Venus thermosphere densities as revealed by Venus Express Torque and Accelerometer data. Master Thesis, Luleå Univ. of Technology.

Piccialli, A., Montmessin, F., Belyaev, D., Mahieux, A., Fedorova, A., Marcq, E., Bertaux, J.L., Tellmann, S., Vandaele, A.C., Korablev, O., 2015. Thermal structure of Venus nightside upper atmosphere measured by stellar occultations with SPICAV/Venus Express. *Planetary and Space Science* 113, 321–335. doi:10.1016/j.pss.2014.12.009.

Ponder, B.M., Ridley, A.J., Bouger, S.W., Pawlowski, D., Brecht, A., 2024. The venus global ionosphere-thermosphere model (v-gitm): A coupled thermosphere and ionosphere formulation. *Journal of Geophysical Research: Planets* 129, e2023JE008079. URL: <https://agupubs.onlinelibrary.wiley.com/doi/abs/10.1029/2023JE008079>, doi:<https://doi.org/10.1029/2023JE008079>, arXiv:<https://agupubs.onlinelibrary.wiley.com/doi/abs/10.1029/2023JE008079> 2023JE008079.

Rengel, M., Hartogh, P., Jarchow, C., 2008. Mesospheric vertical thermal structure and winds on Venus from HHSMT CO spectral-line observations. *Planetary and Space Science* 56, 1368–1384. doi:10.1016/j.pss.2008.07.004, arXiv:0809.2743.

Richards, P.C., Fennelly, J.A., Torr, D.G., 1994. EUVAC: a solar EUV flux model for aeronomic calculations. *Journal of Geophysical Research* 99, 8981–8992.

Richmond, A.D., Ridley, E.C., Roble, R.G., 1992. A thermosphere/ionosphere general circulation model with coupled electrodynamics. *Geophysical Research Letters* 19, 601–604. doi:10.1029/92GL00401.

Ridley, A.J., Deng, Y., Tóth, G., 2006. The global ionosphere thermosphere model. *Journal of Atmospheric and Solar-Terrestrial Physics* 68, 839–864. doi:10.1016/j.jastp.2006.01.008.

Roble, R.G., Ridley, E.C., Richmond, A.D., Dickinson, R.E., 1988. A coupled thermosphere/ionosphere general circulation model. *Geophysical Research Letters* 15, 1325–1328. doi:10.1029/GL015i012p01325.

Roldán, C., López-Valverde, M.A., López-Puertas, M., Edwards, D.P., 2000. Non-LTE Infrared Emissions of CO<sub>2</sub> in the Atmosphere of Venus. *Icarus* 147, 11–25. doi:doi = 10.1006/icar.2000.6432,.

Rozelot, J.P., Damiani, C., Lefebvre, S., 2009. New findings increasing solar trend that can change earth climate. *Proceedings of the International Astronomical Union* 5, 301–309. doi:10.1017/S1743921309992845.

Schubert, G., Bouger, S.W., Covey, C.C., Del Genio, A.D., Grossman, A.S., Hollingsworth, J.L., Limaye, S.S., Young, R.E., 2007. Venus Atmosphere Dynamics: A Continuing Enigma. American Geophysical Union (AGU). pp. 101–120. URL: <https://agupubs.onlinelibrary.wiley.com/doi/abs/10.1029/176GM07>, doi:<https://doi.org/10.1029/176GM07>.

Schubert, G., Covey, C., del Genio, A., Elson, L.S., Keating, G., Seiff, A., Young, R.E., Apt, J., Counselman, C.C., Kliore, A.J., Limaye, S.S., Revercomb, H.E., Sromovsky, L.A., Suomi, V.E., Taylor, F., Woo, R., von Zahn, U., 1980. Structure and circulation of the Venus atmosphere. *Journal of Geophysical Research* 85, 8007–8025. doi:10.1029/JA085iA13p08007.

Schunk, R., Nagy, A., 2009. Ionospheres: Physics, Plasma Physics, and Chemistry. doi:10.1017/CBO9780511635342.

Seiff, A., Schofield, J.T., Kliore, A.J., Taylor, F.W., Limaye, S.S., 1985. Models of the structure of the atmosphere of Venus from the surface to 100 kilometers altitude. *Advances in Space Research* 5, 3–58. doi:10.1016/0273-1177(85)90197-8.

Solomon, S.C., Qian, L., 2005. Solar extreme-ultraviolet irradiance for general circulation models. *Journal of Geophysical Research (Space Physics)* 110, A10306. doi:10.1029/2005JA011160.

Stief, L.J., De Carlo, V.J., Payne, W.A., 1969. Xenon sensitized photolysis of carbon dioxide. *The Journal of Chemical Physics* 51, 3336–3341. URL: <https://doi.org/10.1063/1.1672516>, doi:10.1063/1.1672516.

Stolzenbach, A., Lefèvre, F., Lebonnois, S., Määttänen, A., 2023. Three-dimensional modeling of Venus photochemistry and clouds. *Icarus* 395, 115447. doi:10.1016/j.icarus.2023.115447.

Sugimoto, N., Takagi, M., Matsuda, Y., 2014. Waves in a Venus general circulation model. *Geophysical Research Letters* 41, 7461–7467. doi:10.1002/2014GL061807.

Tobiska, W.K., Woods, T., Eparvier, F., Viereck, R., Floyd, L., Bouwer, D., Rottman, G., White, O.R., 2000. The SOLAR2000 empirical solar irradiance model and forecast tool. *J. Atmos. Solar-Terr. Phys.* 62, 1233–1250.

Tolson, R.H., Prince, J., Konopliv, A., 2013. An atmospheric variability model for venus aerobraking missions. AIAA Modeling and Simulation Technologies (MST) Conference URL: <https://arc.aiaa.org/doi/abs/10.2514/6.2013-4830>, doi:10.2514/6.2013-4830.

Torr, M.R., Torr, D.G., 1985. Ionization frequencies for solar cycle 21: Revised. *Journal of Geophysical Research* 90, 6675–6678. doi:10.1029/JA090iA07p06675.

Torr, M.R., Torr, D.G., Ong, R.A., Hinteregger, H.E., 1979. Ionization frequencies for major thermospheric constituents as a function of solar cycle 21. *Geophysical Research Letters* 6, 771–774. doi:10.1029/GL006i010p00771.

Vandaele, A.C., Mahieux, A., Chamberlain, S., Ristic, B., Robert, S., Thomas, I.R., Trompet, L., Wilquet, V., Bertaux, J.L., 2016. Carbon monoxide observed in Venus' atmosphere with SOIR/VEx. *Icarus* 272, 48–59. doi:10.1016/j.icarus.2016.02.025.

Woods, T.N., Eparvier, F.G., Harder, J., Snow, M., 2018. Decoupling Solar Variability and Instrument Trends Using the Multiple Same-Irradiance-Level (MuSIL) Analysis Technique. *Solar Physics* 293, 76. doi:10.1007/s11207-018-1294-5.

Woods, T.N., Rottman, G.J., 2002. Solar Ultraviolet Variability Over Time Periods of Aeronomic Interest. *Geophysical Monograph Series* 130, 221. doi:10.1029/130GM14.

Yamamoto, M., 2019. Equatorial kelvin-like waves on slowly rotating and/or small-sized spheres: Application to venus and titan. *Icarus* 322, 103–113.

Young, R.E., Pollack, J.B., 1977. A three-dimensional model of dynamical processes in the Venus atmosphere. *Journal of the Atmospheric Sciences* 34, 1315–1351. doi:10.1175/1520-0469(1977)034j1315:ATMODP;2.0.CO;2.

Yung, Y.L., Demore, W.B., 1982. Photochemistry of the stratosphere of Venus - Implications for atmospheric evolution. *Icarus* 51, 199–247. doi:10.1016/0019-1035(82)90080-X.